

# Multimodal Classification Network Guided Trajectory Planning for Four-Wheel Independent Steering Autonomous Parking Considering Obstacle Attributes

Jingjia Teng<sup>a</sup>, Yang Li<sup>a</sup>, Jianqiang Wang<sup>b</sup>, Yingbai Hu<sup>c</sup>, Songyuan Tang<sup>a</sup> and Manjiang Hu<sup>a,\*</sup>

<sup>a</sup>College of Mechanical and Vehicle Engineering, Hunan University, Changsha 410082, China.

<sup>b</sup>The State Key Laboratory of Automotive Safety and Energy, Tsinghua University, Beijing 100084, China.

<sup>c</sup>The Multi-Scale Medical Robotics Centre, the Chinese University of Hong Kong, Shatin 999077, China.

## ARTICLE INFO

### Keywords:

Four-Wheel Independent Steering  
Trajectory planning  
Obstacle attributes  
Risk field  
Optimal control problem

## ABSTRACT

Four-wheel Independent Steering (4WIS) vehicles have attracted increasing attention for their superior maneuverability. Human drivers typically choose to cross or drive over the low-profile obstacles (*e.g.*, plastic bags) to efficiently navigate through narrow spaces, while existing planners neglect obstacle attributes, causing inefficiency or path-finding failures. To address this, we propose a trajectory planning framework integrating the 4WIS hybrid A\* and Optimal Control Problem (OCP), in which the hybrid A\* provides an initial path to enhance the OCP solution. Specifically, a multimodal classification network is introduced to assess scene complexity (hard/easy task) by fusing image and vehicle state data. For hard tasks, guided points are set to decompose complex tasks into local subtasks, improving the search efficiency of 4WIS hybrid A\*. The multiple steering modes of 4WIS vehicles—Ackermann, diagonal, and zero-turn—are also incorporated into node expansion and heuristic designs. Moreover, a hierarchical obstacle handling strategy is designed to guide the node expansion considering obstacle attributes, *i.e.*, “non-traversable”, “crossable”, and “drive-over” obstacles. It allows crossing or driving over obstacles instead of the “avoid-only” strategy, greatly enhancing success rates of pathfinding. We also design a logical constraint for the “drive-over” obstacle by limiting its velocity to ensure safety. Furthermore, to address dynamic obstacles with motion uncertainty, we introduce a probabilistic risk field model, constructing risk-aware driving corridors that serve as linear collision constraints in OCP. Experimental results demonstrate the proposed framework’s effectiveness in generating safe, efficient, and smooth trajectories for 4WIS vehicles, especially in constrained environments.

## 1. Introduction

### 1.1. Background

Four-Wheel Independent Steering (4WIS) vehicles are capable of independently controlling each wheel’s steering angle and have multiple maneuvering modes, including Ackermann steering, diagonal motion, and zero-turn rotation [1]. These diverse motion modes can significantly enhance vehicle maneuverability and improve navigation in narrow environments. Trajectory planning for autonomous vehicles has attracted considerable attention [2], but existing methods do not fully exploit the superior maneuverability of 4WIS vehicles [3, 4, 5], limiting their performance in constrained spaces. Besides, most trajectory planning algorithms intend to avoid all obstacles, regardless of the obstacle attributes [6, 7], which reduces planning efficiency with “crossable” or “drive-over” obstacles such as tiny rocks, cardboard boxes, or speed bumps. Moreover, the motion uncertainty of dynamic obstacles is rarely considered in existing planning frameworks.

Many studies have been proposed to address the above challenges. For instance, [2, 8, 9] proposed improved A\* methods for differential wheeled vehicles. However, these studies typically define motion mode transitions at each node, resulting in trajectories that might violate kinematic constraints. [2] incorporated numerical methods for trajectory optimization into the A\* framework, but it may suffer from poor solution quality and low efficiency in complex environments. [10] focuses on local logical constraints for “drive-over” obstacles, such as speed bumps. However, most

\*Corresponding author. E-mail: lyxc56@gmail.com.

\*\*This work is supported by the National Natural Science Foundation of China under grant 52302493.

studies failed to comprehensively account for all obstacle attributes such as “non-traversable”, “crossable”, and “drive-over” obstacles during both search and optimization stages. Furthermore, [11, 12, 13] studied motion uncertainties of dynamic obstacles for trajectory planning, but those studies relied on intricate uncertainty modeling with high-dimensional probability distributions, which incur high computational overheads and degrade real-time performance.

This study proposes a trajectory planning framework for 4WIS vehicles in narrow and obstacle-dense environments, as illustrated in Fig. 1, accounting for obstacle properties and uncertainty modeling. In Fig. 2, the framework first incorporates a Multimodal Classification Network (MCN) that determines the necessity of guided points, and a Guided Point (GP) generation strategy is developed to assist the hybrid A\* algorithm. The 4WIS hybrid A\* algorithm can integrate multiple kinematic modes with customized heuristic functions, and a hierarchical obstacle handling strategy considering obstacle attributes is implemented to enhance search efficiency. Finally, a trajectory optimization module is formulated, constructing probabilistic risk field-based driving corridors to handle the motion uncertainty of dynamic obstacles and introducing logical constraints for “drive-over” static obstacles. To enhance optimization efficiency, the trajectory generated by the 4WIS hybrid A\* serves as a warm start for the trajectory optimization. The main contributions are summarized as follows:

- A multimodal classification network is built to assess the scene complexity (hard/easy) based on the fusion of image and state data, and an auxiliary alignment loss is designed to enforce consistency between image and state embeddings. Guided points are set for the hard task to enhance the search efficiency of hybrid A\* by decomposing the complex planning task into simple subtasks.
- A 4WIS hybrid A\* algorithm is developed to exploit Ackermann steering, diagonal movement, and zero-turn rotation modes, and incorporate these motion modes into the node expansion process by computing candidate trajectories based on their kinematic equations. Node cost and mode switching cost are also designed to reduce unnecessary reversals and frequent mode switches.
- We introduce a hierarchical obstacle handling strategy into the 4WIS hybrid A\* framework, which determines the expansion direction based on obstacle attributes to improve planning efficiency in scenarios with dense obstacles. This strategy prioritizes crossing when feasible, and otherwise selects to drive over or avoid obstacles.
- A probabilistic risk field-based driving corridor method is proposed that accounts for the motion uncertainty of dynamic obstacles and formulates linear collision avoidance constraints to reduce complexity. In addition, logical constraints for “drive-over” obstacles are incorporated to ensure safety by limiting the vehicle’s velocity.

## 1.2. Related Works

**Motion Planning.** Search-based methods explore the state space using heuristic algorithms to generate feasible trajectories.[14] proposed the Neural Network-based Path Proposal (NNPP) model to guide A\* search in rough terrains.[15] presented the hybrid A\* algorithm, which integrates discrete search with continuous space. [16] proposed a fault-tolerant hybrid A\* (FTHA) algorithm that ensures completeness by falling back to A\*, but the path may violate kinematic constraints. [17] proposed a goal ordering strategy with an improved A\* to enhance multi-goal path planning efficiency.[18] proposed guide points to increase search efficiency. Optimization-based methods formulate trajectory planning as an optimization problem, using numerical techniques to generate a feasible trajectory. [19] introduced the Convex Feasible Set algorithm for fast local convergence.[20] proposed a trajectory planning method for 2.5D environments. [21] proposed a rapid iterative trajectory planning method based on path velocity decomposition to improve efficiency and control feasibility in automated parking.[22] formulated the trajectory planning task as a mixed-integer nonlinear programming problem. Different from existing studies, we propose a multimodal classification network-guided trajectory planning framework that determines the necessity of guided points. A guided points generation strategy is designed to decompose the complex planning task into local subtasks, improving planning efficiency in cluttered environments. The initial path then serves as a warm start for solving the OCP to obtain an optimal trajectory.

**4WIS Vehicle Motion Planning.** Most existing motion planning studies are developed for conventional front-wheel drive vehicles, with limited attention given to 4WIS systems. [8] proposed an improved A\* algorithm for differential wheeled vehicles. [5] proposed an A\*-based energy-efficient planner for Ackermann vehicles using energy-aware motion primitives. [23] presented a B-spline-based trajectory planning method for smooth steering mode switching in 4WIS vehicles. [24] presented a kinematics-based trajectory planning algorithm for 4WIS vehicles,

focusing on steering and velocity planning. [1] integrated Reeds-Shepp curves and optimal control to enhance efficiency and adapt to dynamic obstacles for 4WIS vehicles. [25] presented a clothoid-based trajectory planning method for 4WIS-4WID vehicles to enable active collision avoidance. Different from existing studies, we develop a 4WIS hybrid A\* algorithm that explicitly incorporates Ackermann steering mode, diagonal movement mode, and zero-turn rotation mode.

**Obstacle Handling Strategy.** Handling obstacles requires a balance between the solution quality and computational efficiency. Static obstacles are among the most prevalent obstacles in autonomous driving environments. [26] used a Voronoi-based roadmap and tunnel constraints to handle “non-traversable” obstacles. [20] proposed a trajectory planning framework for “drive-over” obstacles like road shoulders and slopes. [27] proposed a double-layer collision checking method for “crossable” obstacles. To handle dynamic obstacles, [28] modeled obstacle motion and position uncertainties using Gaussian distributions. [11] enhanced reachable set generation by integrating collision probabilities. [12] used a Linear Quadratic Gaussian framework to enhance robustness under prediction uncertainty. [29] modeled risks for static and dynamic obstacles, while [13] extended it with a time-series motion risk field for spatiotemporal mapping. Different from existing studies, we integrate a hierarchical obstacle handling strategy into the 4WIS hybrid A\* framework, selecting expansion directions based on obstacle attributes. For dynamic obstacles, we propose a probabilistic risk field-based corridor method that accounts for motion uncertainty. Logical constraints for “drive-over” obstacles are also introduced to limit vehicle velocity to enhance stability.

## 2. Problem Formulation

### 2.1. Vehicle Kinematic Model

Three motion modes of the 4WIS vehicle, including Ackermann steering mode, diagonal movement mode, and zero-turn rotation mode, are incorporated into the planning framework.

**Ackermann steering mode.** The 4WIS vehicle performs curvilinear motion while satisfying Ackermann steering geometry constraints, as shown in Fig. 3(a). The kinematic model can be described:

$$\begin{bmatrix} \dot{x}(t) \\ \dot{y}(t) \\ \dot{v}(t) \\ \dot{\theta}(t) \\ \dot{\delta}(t) \end{bmatrix} = \begin{bmatrix} v(t) \cdot \cos \theta(t) \\ v(t) \cdot \sin \theta(t) \\ a(t) \\ 2v(t) \cdot \tan \delta(t) / L_w \\ \omega_\delta(t) \end{bmatrix}, t \in [0, t_f], \quad (1)$$

where  $x(t)$  and  $y(t)$  denote the longitudinal and lateral coordinates of the vehicle center point, respectively, and  $v(t)$  is the velocity,  $\theta(t)$  is the heading angle,  $\delta(t)$  is the front-wheel steering angle.  $a(t)$  is the acceleration,  $L_w$  is the vehicle wheelbase,  $\omega_\delta(t)$  is the front wheel angular velocity,  $t_f$  is the planning duration.

**Diagonal movement mode.** All wheels steer at the same angle  $\delta(t)$ , while the vehicle’s orientation  $\theta(t)$  remains constant, enabling motion along the direction  $(\theta(t) + \delta(t))$ , as shown in Fig. 3(b). The kinematic model can be described:

$$\begin{bmatrix} \dot{x}(t) \\ \dot{y}(t) \\ \dot{v}(t) \\ \dot{\theta}(t) \\ \dot{\delta}(t) \end{bmatrix} = \begin{bmatrix} v(t) \cdot \cos(\theta(t) + \delta(t)) \\ v(t) \cdot \sin(\theta(t) + \delta(t)) \\ a(t) \\ 0 \\ 0 \end{bmatrix}, t \in [0, t_f]. \quad (2)$$

**Zero-turn rotation mode.** The vehicle steers around the center point, and the orientation angle  $\theta$  is changing, as shown in Fig. 3(c). The kinematic model can be described:

$$\begin{bmatrix} \dot{x}(t) \\ \dot{y}(t) \\ \dot{v}(t) \\ \dot{\theta}(t) \\ \dot{\delta}(t) \end{bmatrix} = \begin{bmatrix} 0 \\ 0 \\ 0 \\ \omega_\theta \\ 0 \end{bmatrix}, t \in [0, t_f], \quad (3)$$

where  $\omega_\theta$  is the yaw rate, assumed to be constant in this study.

## 2.2. Optimal Control Problem

### 2.2.1. Cost Function

Trajectory planning is formulated as an OCP, with a cost function that considers the planning efficiency, driving comfort, and smoothness:

$$J_c = \lambda_1 \cdot t_f + \lambda_2 \cdot \int_0^{t_f} (a^2(\tau) + \delta^2(\tau) + w_\delta^2(\tau)) \cdot d\tau, \quad (4)$$

where  $\lambda_1$  and  $\lambda_2$  are weighting coefficients.

### 2.2.2. Collision Avoidance Constraint

Referring to [16], the driving corridor approach is used to linearize the collision avoidance constraints and improve computational efficiency. [16] uses a fixed step size, and a large step size may lead to suboptimal solutions, while a small step size increases computational cost. To address this, an adaptive step size strategy is designed, as illustrated in Fig. 4. The expansion starts from the sampling point (yellow dot) and the expansion is performed in four directions: upward, rightward, downward, and leftward, and the step size is dynamically adjusted based on the outcomes of each expansion. After each expansion in a given direction, the step size for the next expansion is updated. A successful expansion indicates that a sufficient space remains, while a failed expansion indicates a collision with the obstacle (see Fig. 4). The number of failed expansions is recorded, and once it reaches a predefined threshold in a given direction, expansion along that direction is terminated. Let  $(x(j), y(j))$  be the current sampling point, and the expansion distance  $l_j^R$  ( $R \in \{\text{upward, rightward, downward, leftward}\}$ ) in each direction is used to represent the driving corridor  $C_j$ :

$$\begin{cases} C_j = \{(x, y) \mid \mathcal{E}_j^{\text{left}} \leq x \leq \mathcal{E}_j^{\text{right}}, \mathcal{E}_j^{\text{down}} \leq y \leq \mathcal{E}_j^{\text{up}}\}, \\ \mathcal{E}_j^{\text{up}} = y(j) + l_j^{\text{up}}, \quad \mathcal{E}_j^{\text{down}} = y(j) - l_j^{\text{down}}, \\ \mathcal{E}_j^{\text{right}} = x(j) + l_j^{\text{right}}, \quad \mathcal{E}_j^{\text{left}} = x(j) - l_j^{\text{left}}, \end{cases} \quad (5)$$

where  $\mathcal{E}_j^{\text{up}}$ ,  $\mathcal{E}_j^{\text{right}}$ ,  $\mathcal{E}_j^{\text{down}}$ , and  $\mathcal{E}_j^{\text{left}}$  denote the boundaries of the driving corridor in each direction.

### 2.2.3. Boundary Conditions Constraints

It defines the initial state constraint and terminal constraint. The trajectory is discretized as  $\{s(0), s(1), \dots, s(N_f)\}$ ,  $N_f = t_f / \Delta t$ ,  $\Delta t$  is the sampling time interval. The boundary conditions is described as:

$$s(0) = s_{t_0}, \quad s(N_f) = s_{t_f}, \quad (6)$$

where  $s(0)$  and  $s(N_f)$  are initial state and terminal state.  $s_{t_0}$  and  $s_{t_f}$  represent the initial and goal state variables.

### 2.2.4. Optimization Model

The trajectory planning problem can be written as the following OCP:

$$\begin{aligned} \min \quad & J_c \\ \text{s.t.} \quad & \text{Vehicle Kinematic Constraints: (1), (2), (3),} \\ & \text{Collision Avoidance Constraints: (5),} \\ & \text{Boundary Conditions Constraints: (6),} \end{aligned} \quad (7)$$

where the cost function is  $J_c$ , and vehicle kinematic constraints, boundary condition constraints, and collision avoidance constraints are included.

## 3. Guided Points Generation Strategy

### 3.1. Visible Points

We employ the A\* algorithm to generate a feasible path from the initial state to the goal state. Let  $P = \{p_i\}_{i=1}^N$  be the waypoints along this path, and  $p_i = (p_{i,x}, p_{i,y})$  denote a discrete waypoint,  $N$  is the number of points. The A\* path

implicitly contains environmental information, such as obstacle locations and available free space. To set the guided points, we define the visible points (see Fig. 5(a)) as follows.

**Visible Points.** Consider an environment with obstacle space  $O_{\text{obs}} \subseteq \mathbb{R}^2$  and a free space  $O_{\text{free}} \subseteq \mathbb{R}^2$ . Let  $p_A \in O_{\text{free}}$  and  $p_B \in O_{\text{free}}$  be two points in the free space. The line segment connecting  $p_A$  and  $p_B$  is defined as  $l_{A,B} = \{(1-\lambda)p_A + \lambda p_B \mid 0 \leq \lambda \leq 1\}$ . If  $l_{A,B} \cap O_{\text{obs}} = \emptyset$ , then the point  $p_B$  is defined as a visible point of  $p_A$ . All visible points of a point  $p_A$  are stored in  $P_A^{\text{vis}} = \{p_i\}_{i=1}^{N_v}$ ,  $N_v$  is the number of visible points for the point  $p_A$ .

**Farthest Visible Point.** If  $\exists p_f \in P_A^{\text{vis}}, \forall p_j \in P_A^{\text{vis}} (j \neq f)$ , it holds  $\|l_{p_A, p_f}\| \geq \|l_{p_A, p_j}\|$ , then the point  $p_f$  is defined as the farthest visible point of a point  $p_A$ . We denote the farthest visible point as  $p_f = \mathcal{F}(p_A)$ ,  $\mathcal{F}$  is the mapping function. The  $k$ -th recursive operation of this mapping is denoted as  $\mathcal{F}^k(p_A)$ , and satisfies:

$$\mathcal{F}^0(p_A) \triangleq p_A, \quad \mathcal{F}^{k+1}(p_A) \triangleq \mathcal{F}(\mathcal{F}^k(p_A)).$$

**Consecutive Farthest Visible Point Set.** The consecutive farthest visible point set from  $p_1$  to  $p_N$  is denoted as  $V_{p_1} = \{p_1, \mathcal{F}_p^1(p_1), \dots, \mathcal{F}^m(p_1)\}$ ,  $m \in \mathbb{Z}$ ,  $1 \leq m \leq N$ ,  $\mathcal{F}^m(p_1) = p_N$ ,  $|V_{p_1}| = m + 1$ . The process of generating the consecutive farthest visible point set  $V_{p_1}$  along the A\* path is detailed in Algorithm A.1 (see Appendix A).

### 3.2. Gear Shifting Points

The gear shifting point is essential in setting the guided points. We first evaluate whether gear shifting is required and then identify the region along the A\* path that finds the largest free space to set the gear shifting point. As shown in Fig. 5,  $\alpha_1$  and  $\alpha_2$  are defined as the angles between the vehicle's initial and goal orientations and the A\* path, respectively. If  $\cos \alpha_1 \cdot \cos \alpha_2 > 0$ , we assume that the vehicle can proceed directly without gear shifting. In contrast, if  $\cos \alpha_1 \cdot \cos \alpha_2 \leq 0$ , we assume that the gear shifting is required. We determine the appropriate shifting point only when gear shifting is required. Starting from the consecutive farthest visible point  $V_{p_1}$ , we expand outward in all directions at each point in  $V_{p_1}$ —similar to constructing a driving corridor—to form a series of local rectangular regions along the A\* path. These local rectangles are denoted as  $\mathcal{D} = \{\mathcal{D}p_1, \mathcal{D}p_2, \dots, \mathcal{D}p_N\}$ . To improve the feasibility of gear shifting, the largest rectangle among them is selected for determining the gear shifting point, as illustrated in Fig. 5(b). The intersection points between this largest rectangle and the A\* path are denoted as  $p_{I_1}$  and  $p_{I_2}$ . To ensure smooth transition and trajectory continuity, two clothoid curves are constructed based on  $p_{I_1}$  and  $p_{I_2}$ , respectively. The gear shifting point  $p_g$  is defined as the intersection of these two clothoid curves, which can be obtained by solving the following equations:

$$C(\theta_{p_{I_1}}, R_{\min}, l_{\text{curve}}) = C(\theta_{p_{I_2}}, R_{\min}, l_{\text{curve}}), \quad (8)$$

where  $C(\cdot)$  denotes the clothoid curve parameterized by the heading angle, minimum turning radius  $R_{\min}$ , and curve length  $l_{\text{curve}}$ .  $\theta_{p_{I_1}}$  and  $\theta_{p_{I_2}}$  are the heading angles of the two points  $p_{I_1}$  and  $p_{I_2}$ , respectively.

### 3.3. Generation of Guided Points

The gear shifting point  $p_g$  is a special guided point when gear shifting is needed. In addition, the guided points are selected at the center of each rectangle in  $\mathcal{D} = \{\mathcal{D}p_1, \mathcal{D}p_2, \dots, \mathcal{D}p_N\}$ . We use  $(g_{i,x}, g_{i,y})$  to denote the position of the guided point  $g_i$ . Moreover, each guided point  $g_i$  is assigned an orientation angle  $\theta_{g_i}$  based on the angles  $\alpha_1$  and  $\alpha_2$ . Four cases are considered:

**Case 1:**  $\cos \alpha_1 > 0, \cos \alpha_2 > 0$ . The vehicle can reach the goal by moving *forward* without gear shifting:

$$\theta_{g_i} = \text{atan2}(g_{i+1,y} - g_{i,y}, g_{i+1,x} - g_{i,x}) \quad (9)$$

**Case 2:**  $\cos \alpha_1 < 0, \cos \alpha_2 < 0$ . The vehicle can *reverse* to the goal without gear shifting:

$$\theta_{g_i} = \text{atan2}(g_{i,y} - g_{i+1,y}, g_{i,x} - g_{i+1,x}) \quad (10)$$

**Case 3:**  $\cos \alpha_1 \geq 0, \cos \alpha_2 \leq 0$ . Gear shifting is required. The vehicle moves *forward* between the initial state  $X_s$  and  $p_g$ , and *reverses* between  $p_g$  and the goal state  $X_f$ :

$$\theta_{g_i} = \begin{cases} \text{atan2}(g_{i+1,y} - g_{i,y}, g_{i+1,x} - g_{i,x}), & \text{if } g_i \in [X_s, p_g], \\ \text{atan2}(g_{i,y} - g_{i+1,y}, g_{i,x} - g_{i+1,x}), & \text{otherwise.} \end{cases} \quad (11)$$

**Case 4:**  $\cos \alpha_1 < 0$ ,  $\cos \alpha_2 > 0$ . Gear shifting is required. The vehicle *reverses* between  $X_s$  and  $p_g$ , and moves *forward* between  $p_g$  and  $X_f$ :

$$\theta_{g_i} = \begin{cases} \text{atan2}(g_{i,y} - g_{i+1,y}, g_{i,x} - g_{i+1,x}), & \text{if } g_i \in [X_s, p_g], \\ \text{atan2}(g_{i+1,y} - g_{i,y}, g_{i+1,x} - g_{i,x}), & \text{otherwise.} \end{cases} \quad (12)$$

The guided points  $g_i$  are represented as  $(g_{i,x}, g_{i,y}, \theta_{g_i})$ , which are used to instruct the hybrid A\* algorithm by decomposing the complex planning task into local subtasks.

## 4. Multimodal Classification Network

Applying the guided point strategy to simple tasks may incur unnecessary computational overhead. To address this, we introduce a multimodal classification network to assess scenario complexity. The guided point generation strategy is activated only when the scenario is classified as a hard planning task. As illustrated in Fig. 6, the multimodal classification network employs a fusion architecture that integrates both visual and state information. Specifically, ResNet-18 is utilized to extract features from scenario images, while a multilayer perceptron (MLP) encodes vehicle state data. Additionally, the pixel proportions of semantic regions are incorporated as supplementary inputs. These diverse features are concatenated and passed through a classification head to assess scenario complexity, categorizing it as either “hard” or “easy”. Moreover, to enhance semantic alignment between image and state features, an auxiliary loss function is introduced, thereby promoting more coherent feature representations.

### 4.1. Model Architecture

Our model takes the scenario image and the vehicle states as input, and outputs the classification result, *i.e.*, hard/easy planning task, as illustrated in Fig. 6. Scenario images are generated through simulation, with distinct colors used to annotate key elements such as the initial state, goal state, obstacles, and free space. The vehicle state data includes the initial and goal state of the vehicle, represented as  $X_s = (x_s, y_s, \theta_s)$  and  $X_f = (x_f, y_f, \theta_f)$ , respectively.

**Initial Mask, Goal Mask, and Obstacle Mask.** To capture the spatial distribution of the initial state, the goal state, and obstacles in the image, we define the initial mask indicator function  $\mathbb{1}_{\text{init}}(i, j)$ , the goal mask indicator function  $\mathbb{1}_{\text{goal}}(i, j)$ , and the obstacle mask indicator function  $\mathbb{1}_{\text{obs}}(i, j)$  based on the color of the pixel:

$$\mathbb{1}_{\text{init}}(i, j) = \begin{cases} 1, & \text{if } P(i, j) = (255, 0, 255), \\ 0, & \text{otherwise.} \end{cases} \quad (13)$$

$$\mathbb{1}_{\text{goal}}(i, j) = \begin{cases} 1, & \text{if } P(i, j) = (0, 255, 0), \\ 0, & \text{otherwise.} \end{cases}, \quad \mathbb{1}_{\text{obs}}(i, j) = \begin{cases} 1, & \text{if } P(i, j) = (0, 0, 0), \\ 0, & \text{otherwise.} \end{cases} \quad (14)$$

where  $P(i, j)$  is the pixel value.  $P(i, j) = (255, 0, 255)$  indicates that the pixel is magenta, which is the initial state;  $P(i, j) = (0, 255, 0)$  indicates that the pixel is green, which is the goal state;  $P(i, j) = (0, 0, 0)$  indicates that the pixel is black, which is the obstacle. Next, we compute the number of pixels located in the initial state, the goal state, and the obstacle areas in the image:

$$N_{\mathcal{M}} = \sum_{i=1}^W \sum_{j=1}^H \mathbb{1}_{\mathcal{M}}(i, j), \quad \mathcal{M} \in \{\text{init, goal, obs}\}, \quad (15)$$

where  $N_{\mathcal{M}}$  represents the total number of pixels within the region  $\mathcal{M}$ , where  $\mathcal{M} \in \{\text{init, goal, obs}\}$  corresponds to the initial state, goal state, and obstacle area, respectively.  $H$  and  $W$  are the height and width of the image, respectively. The total number of pixels in the scenario image  $N_{\text{total}} = W \times H$  is also computed. The proportions of the initial state region, goal state region, and obstacle region in the entire image are represented by  $\frac{N_{\text{init}}}{N_{\text{total}}}$ ,  $\frac{N_{\text{goal}}}{N_{\text{total}}}$ , and  $\frac{N_{\text{obs}}}{N_{\text{total}}}$ , respectively. Simultaneously, these proportions are processed with an MLP separately to extract feature representations:

$$F_{\mathcal{M}}^r = \text{MLP} \left( \frac{N_{\mathcal{M}}}{N_{\text{total}}} \right), \quad \mathcal{M} \in \{\text{init, goal, obs}\}, \quad (16)$$

where each  $F_{\mathcal{M}}^r$  is an extracted ratio feature representation.

**Image Feature Extraction.** Simultaneously, the raw RGB image is passed through a pre-trained ResNet-18 backbone to extract deep visual features  $F^{\text{img}}$  [30]. The input image is denoted as  $I \in \mathbb{R}^{H \times W \times 3}$  and the image feature representation  $F^{\text{img}}$  is written as:

$$F^{\text{img}} = \text{ResNet18}(I). \quad (17)$$

**Vehicle State Feature Extraction.** Simultaneously, the initial state  $X_s$  and goal state  $X_f$  are processed with MLP separately to extract individual feature representations:

$$F_{\text{init}}^{\text{state}} = \text{MLP}(X_s), \quad F_{\text{goal}}^{\text{state}} = \text{MLP}(X_f), \quad (18)$$

where  $F_{\text{init}}^{\text{state}}$  and  $F_{\text{goal}}^{\text{state}}$  are feature vectors extracted from the initial and goal states, respectively.

**Multi-modal Feature Fusion.** The image features  $F^{\text{img}}$ , initial state features  $F_{\text{init}}^{\text{state}}$ , goal state features  $F_{\text{goal}}^{\text{state}}$ , initial state ratio features  $F_{\text{init}}^r$ , goal state ratio features  $F_{\text{goal}}^r$  and obstacle ratio features  $F_{\text{obs}}^r$  are concatenated together to form a combined feature vector  $F_c$ :

$$F_c = \text{Concat}(F^{\text{img}}, F_{\text{init}}^{\text{state}}, F_{\text{goal}}^{\text{state}}, F_{\text{init}}^r, F_{\text{goal}}^r, F_{\text{obs}}^r) \quad (19)$$

Here,  $F_c$  is subsequently passed through two fully connected (Linear) layers with a ReLU activation in between, followed by a Sigmoid output layer producing  $\hat{Y}$ , which classifies whether the task at hand is a ‘‘Hard Task’’ (Yes/No):

$$\hat{Y} = \text{MLP}(F_c), \quad (20)$$

where  $\hat{Y}$  is the probability of the hard planning task. It is classified as a hard planning task if the probability of the hard task is larger than 0.5.

## 4.2. Loss Function

We combine the standard binary cross-entropy loss with an alignment loss to ensure both classification accuracy and meaningful spatial embeddings. The binary cross-entropy loss  $\mathcal{L}_{\text{CE}}$  is used for the primary binary classification task:

$$\mathcal{L}_{\text{CE}} = -Y \log(\hat{Y}) - (1 - Y) \log(1 - \hat{Y}), \quad (21)$$

where  $Y$  represents the ground truth label. The alignment loss is defined to align the color features and state features of the initial and goal state regions in the scenario image. We first compute the average pixel values of the initial state and goal state regions:

$$c_{\text{init}} = \frac{\sum_{i=1}^W \sum_{j=1}^H \mathbb{1}_{\text{init}}(i, j) \cdot P(i, j)}{N_{\text{init}}}, \quad c_{\text{goal}} = \frac{\sum_{i=1}^W \sum_{j=1}^H \mathbb{1}_{\text{goal}}(i, j) \cdot P(i, j)}{N_{\text{goal}}}, \quad (22)$$

where  $c_{\text{init}}$  and  $c_{\text{goal}}$  are the average pixel values of the initial state and goal state region, respectively.  $c_{\text{init}}$  and  $c_{\text{goal}}$  are passed through separate fully connected layers to obtain feature embeddings:

$$F_{\text{init}}^{\text{color}} = \text{FC}(c_{\text{init}}), \quad F_{\text{goal}}^{\text{color}} = \text{FC}(c_{\text{goal}}), \quad (23)$$

where  $F_{\text{init}}^{\text{color}}$  and  $F_{\text{goal}}^{\text{color}}$  represent the feature embeddings of the initial and goal state regions, respectively.  $\text{FC}(\cdot)$  is a fully connected layer. To encourage the spatial consistency between the color and state representations, we introduce an auxiliary alignment loss  $\mathcal{L}_{\text{align}}$ :

$$\mathcal{L}_{\text{align}} = \|F_{\text{init}}^{\text{color}} - F_{\text{init}}^{\text{state}}\|_2 + \|F_{\text{goal}}^{\text{color}} - F_{\text{goal}}^{\text{state}}\|_2. \quad (24)$$

The auxiliary alignment loss  $\mathcal{L}_{\text{align}}$  is defined to minimize the mean squared errors between the color features and state features of both the initial and goal state regions. The total loss function  $\mathcal{L}_{\text{total}}$  is defined as the weighted sum of the cross-entropy loss  $\mathcal{L}_{\text{CE}}$  and the alignment loss  $\mathcal{L}_{\text{align}}$ :

$$\mathcal{L}_{\text{total}} = \lambda_{\text{CE}} \mathcal{L}_{\text{CE}} + \lambda_{\text{align}} \mathcal{L}_{\text{align}}, \quad (25)$$

where  $\lambda_{\text{CE}}$  and  $\lambda_{\text{align}}$  are hyperparameters. With the multimodal classification network, our method can adaptively determine whether to utilize guided points based on task complexities. For planning tasks classified as “easy”, guided points are omitted to avoid unnecessary computational overhead. In contrast, for tasks identified as “hard”, guided points are employed to enhance the efficiency and success rate of the 4WIS hybrid A\* algorithm. Overall, this multimodal classification network is supposed to save computation time for “easy” cases and improve the planning efficiency and success rate for “hard” cases.

## 5. 4WIS Hybrid A\* Framework

This section introduces a 4WIS hybrid A\* algorithm that includes three motion modes during node expansion. We set node-cost and mode-switch penalties to reduce unnecessary reversing and frequent switching. Besides, we employ the obstacle attributes to determine the expansion direction to improve path efficiency. Finally, the enhanced 4WIS hybrid A\* that integrates with the guided points and obstacle handling strategies is described.

### 5.1. Heuristic Design

During node expansion of 4WIS hybrid A\*, the parent node is represented as  $n_p = (x_p, y_p, \theta_p, v_p, \delta_p)$  and the child node is  $n_c = (x_c, y_c, \theta_c, v_c, \delta_c)$ . The motion mode of  $n_c$  is  $M(n_c)$ .  $M(n_c) = 1$  represents the Ackermann steering mode,  $M(n_c) = 2$  represents diagonal movement mode, and  $M(n_c) = 3$  represents zero-turn rotation mode. To ensure smooth mode transitions, each child node is evaluated by a comprehensive cost  $F(n_c)$ :

$$F(n_c) = \begin{cases} G(n_c) + H(n_c), & \text{if } M(n_p) = M(n_c), \\ G(n_c) + I(n_c) + H(n_c), & \text{otherwise,} \end{cases} \quad (26)$$

where  $G(n_c)$  denotes the node cost function,  $I(n_c)$  is the mode switching cost, and  $H(n_c)$  is the heuristic cost. If the motion mode of the parent node and the child node is the same,  $F(n_c)$  is defined as the sum of  $G(n_c)$  and  $H(n_c)$ . When  $M(n_p) \neq M(n_c)$ ,  $F(n_c)$  is the sum of  $G(n_c)$ ,  $I(n_c)$ , and  $H(n_c)$ .  $H(n_c)$  is the standard heuristic cost in traditional hybrid A\* [15]. The node cost  $G(n_c)$  and the mode switching cost  $I(n_c)$  are shown below.

#### 5.1.1. Node Cost Function

Different node costs are designed for each child node generated by the three node expansion methods, and the node cost  $G(n_c)$  is described as:

$$G(n_c) = \begin{cases} |v_p - v_c| w_{r,a} + |\delta_p - \delta_c| w_{t,a}, & M(n_c) = 1, \\ |v_p - v_c| w_{r,d} + |\delta_p - \delta_c| w_{t,d}, & M(n_c) = 2, \\ |\theta_p - \theta_c| w_{o,z}, & M(n_c) = 3, \end{cases} \quad (27)$$

where  $w_{r,a}$  and  $w_{t,a}$  are the reversing and steering change penalties for Ackermann steering, respectively;  $w_{r,d}$  and  $w_{t,d}$  are the reversing and steering change penalties for diagonal movement;  $w_{o,z}$  is the orientation change penalty for the zero-turn rotation mode.

#### 5.1.2. Mode Switching Cost Function

While 4WIS vehicles provide flexible maneuverability through multiple motion modes, frequent switching should be penalized. The mode switching cost is defined as:

$$I(n_c) = I_{\text{recover}} + I_{\text{change}}, \quad (28)$$

where  $I_{\text{recover}}$  penalizes resetting the current wheel angle, and  $I_{\text{change}}$  penalizes entering the next motion mode:

$$I_{\text{recover}} = \begin{cases} w_{r,1} \cdot \delta_p, & M(n_p) = 1, \\ w_{r,2} \cdot \delta_p, & M(n_p) = 2, \\ w_{r,3}, & M(n_p) = 3, \end{cases} \quad I_{\text{change}} = \begin{cases} w_{r,1} \cdot \delta_c, & M(n_c) = 1, \\ w_{r,2} \cdot \delta_c, & M(n_c) = 2, \\ w_{r,3} \cdot |\theta_p - \theta_c|, & M(n_c) = 3, \end{cases} \quad (29)$$

where  $w_{r,1}$ ,  $w_{r,2}$  and  $w_{r,3}$  are the penalty coefficients corresponding to Ackermann steering, diagonal movement, and zero-turn rotation, respectively.

## 5.2. Static Obstacle Handling Strategies

To enhance the planning efficiency of the 4WIS hybrid A\* in constrained environments, this study categorizes the static obstacles into “non-traversable”, “crossable”, or “drive-over” obstacles, and sets different node expansion methods for different static obstacles.

### 5.2.1. Obstacle Type

Static obstacles are categorized into three types based on their impacts on the safety of trajectory planning tasks: **Non-traversable obstacles**, such as pedestrians, vehicles, and traffic cones (see Fig.7 (a)), which pose significant collision risks and must be strictly avoided; **Crossable obstacles**, including small rocks or shallow potholes located centrally on the roadway (see Fig.7 (b)), which can be safely passed over if they do not interfere with the vehicle’s wheels or chassis; and **Drive-over obstacles**, such as puddles, speed bumps, and cardboard boxes (see Fig. 7 (c)), which can be driven over at low speeds without compromising vehicle safety.

The “Non-traversable” and “drive-over” obstacles can be readily identified. However, determining “crossable” obstacles is a non-trivial task, as it necessitates evaluating potential collisions with the vehicle’s wheels or chassis. This involves expanding trajectories using the vehicle’s kinematic models, such as (1), (2) and (3), during the node expansion phase of the 4WIS hybrid A\* algorithm, which results in an expanded trajectory set  $T$ . For each trajectory  $T_j \in T$  and the obstacle  $O_i$ , a collision check is performed to determine the feasibility of the path.

First, to assess whether an obstacle collides with the vehicle’s chassis, we define a height-based evaluation function  $f_{\text{height}}(h_{O_i}, h_v)$  that compares the obstacle’s height with the vehicle’s chassis clearance height:

$$f_{\text{height}}(h_{O_i}, h_v) = \begin{cases} 1, & \text{if } h_{O_i} < h_v, \\ 0, & \text{if } h_{O_i} \geq h_v, \end{cases} \quad (30)$$

where  $h_{O_i}$  is the height of obstacle  $O_i$  and  $h_v$  is the vehicle’s ground clearance,  $f_{\text{height}}(h_{O_i}, h_v)$  is a binary variable, in which “0” indicates unsafe, and “1” indicates safe.

Next, to assess whether the obstacle can be crossed without wheel contacts, we define  $f_{\text{wheel}}(T_j, O_i)$  as follows:

$$f_{\text{wheel}}(T_j, O_i) = \begin{cases} 1, & \text{if } \text{proj}(\mathbf{w}(T_j)) \cap \text{proj}(O_i) = \emptyset, \\ 0, & \text{if } \text{proj}(\mathbf{w}(T_j)) \cap \text{proj}(O_i) \neq \emptyset, \end{cases} \quad (31)$$

where  $f_{\text{wheel}}(T_j, O_i)$  is also a binary variable, in which “0” indicates unsafe, and “1” indicates safe.  $\mathbf{w}(T_j)$  is the global position of the vehicle’s wheels along the trajectory  $T_j$ . The operator  $\text{proj}(\cdot)$  denotes the projection onto the  $(x, y)$  plane.  $\text{proj}(\mathbf{w}(T_j))$  is the projected wheel positions and  $\text{proj}(O_i)$  is the projection of the obstacle  $O_i$ . If  $\text{proj}(\mathbf{w}(T_j)) \cap \text{proj}(O_i) = \emptyset$ , it indicates that the obstacle does not overlap with any wheel positions, implying a safe traversal  $f_{\text{passable}}(T_j, O_i) = 1$ . Finally, based on  $f_{\text{height}}(h_{O_i}, h_v)$  and  $f_{\text{wheel}}(T_j, O_i)$ , we can define the function  $f_{\text{crossable}}(T_j, O_i)$  to evaluate whether the ego vehicle can safely cross an obstacle:

$$f_{\text{crossable}}(T_j, O_i) = f_{\text{height}}(h_{O_i}, h_v) \times f_{\text{wheel}}(T_j, O_i), \quad (32)$$

where  $f_{\text{crossable}}(T_j, O_i)$  is a binary variable, in which “0” indicates it cannot be crossed, and “1” indicates it can be safely crossed.  $f_{\text{crossable}}(T_j, O_i) = 1$  when the obstacle does not collide with the vehicle’s chassis or wheels.

### 5.2.2. Obstacle Handling in 4WIS Hybrid A\*

We propose a hierarchical obstacle handling strategy for the node expansion process. First, we determine whether the obstacle is crossable. If the node can directly cross the obstacle without collisions, the node expansion chooses to “cross” the obstacle, and the process terminates. Otherwise, we assess whether the obstacle can be driven over. If “Yes”, it chooses to “drive-over” the obstacle, and the process terminates. However, if neither crossing nor driving over is possible, we test for avoidance. If there exist available free spaces allowing the node to avoid the obstacle, it chooses to “avoid” the obstacle and the process terminates. Finally, if none of the above conditions are met, the node expansion process fails. The process can be formulated:

$$\text{ObstacleHandling}(n_c) = \begin{cases} \text{True}, & \text{succeeds,} \\ \text{False}, & \text{fails.} \end{cases} \quad (33)$$

where  $\text{ObstacleHandling}(n_c)$  denotes the result of node expansion at node  $n_c$ , with *True* indicating a successful expansion and *False* indicating a failure.

**Algorithm 1** Initial Path Generation**Require:** Initial state  $X_s$ , goal state  $X_f$ , and scene image  $I$ 


---

```

1: Initialize: Initial path  $S \leftarrow \emptyset$ ,  $m \leftarrow 1$ ,  $i \leftarrow 1$ 
2: Compute scene_complexity  $\leftarrow f_{\text{mcn}}(X_s, X_f, I)$ 
3: if scene_complexity == “Hard” then
4:   Generate guided points  $G$  and key points  $Q = \{q_i\}_{i=1}^{N_q}$ 
5:   while  $i < N_q$  do
6:     Select one key point  $q_i$  from  $Q$ 
7:      $S_i, m \leftarrow \text{Improved4WISHybridAstar}(i, q_i, Q)$ 
8:     if  $S_i = \emptyset$  then
9:       break ▷ Task fails.
10:    end if
11:    Append segmented path  $S \leftarrow S \cup S_i$ 
12:    Update key points index;  $i \leftarrow m$ 
13:  end while
14: else if scene_complexity == “Easy” then
15:    $S \leftarrow \text{4WISHybridAstar}(X_s, X_f)$  ▷ Easy task.
16: end if
Ensure: initial path  $S$ 

```

---

**5.3. Initial Path Generation**

With the proposed 4WIS hybrid A\*, a initial path can be generated for the OCP. In Algorithm 1, given the initial state  $X_s$ , goal state  $X_f$ , and scene image  $I$ , the scene complexity is assessed using the multimodal classification network function  $f_{\text{mcn}}(X_s, X_f, I)$  (line 2). If the scene is classified as the “Hard” task, the guided point set  $G = \{g_i\}_{i=1}^N$  and the corresponding key point set  $Q = \{q_i\}_{i=1}^{N_q}$ , where  $Q = \{X_s, g_1, g_2, \dots, g_N, X_f\}$ , are employed. In this case, the improved 4WIS hybrid A\* algorithm is used to generate a path segment  $S_i$  from  $q_i$  to a downstream key point in  $Q$  (line 7). If  $S_i \neq \emptyset$ , indicating a successful segment generation, the segment is appended to construct the complete path  $S$ , and the key point index is updated for the next iteration. If  $S_i = \emptyset$ , the process terminates and pathfinding fails. Conversely, if the scene is classified as the “Easy” task, the initial path  $S$  is directly generated using 4WISHybridAstar( $\cdot$ ) (see Algorithm A.2 in Appendix A).

With the guided points, the improved 4WIS hybrid A\* algorithm (Algorithm 2) takes the key point index  $i$ , the corresponding key point  $q_i$ , and the key points set  $Q$  as inputs. The algorithm first attempts to directly connect  $q_i$  to  $q_{i+1}$  (line 2) using either a Reeds–Shepp path or a straight-line segment. If  $\text{TrajConnect}(q_i, q_{i+1}) \neq \emptyset$ , the resulting path and the updated key point index  $m = i + 1$  are returned, and the procedure terminates. When direct connection is not feasible, the algorithm proceeds by expanding the node from  $q_i$ . The key point  $q_i$  is added to the open set  $O$ , and its cost  $F(q_i)$  is stored in the cost set  $\mathcal{F}$ . While the open set  $O$  is not empty and the maximum number of iterations has not been reached, the following steps are performed.

The node  $n_p$  with the lowest cost is selected from  $O$  (line 7), removed from the open set, and added to the closed set  $C$ . Then, expansion is performed by generating a successor node  $n_c$  using an action  $a \in M_s$ , where  $M_s$  denotes the set of motion modes available to 4WIS vehicles. During the expansion process, the hierarchical obstacle-handling strategy is applied via  $\text{ObstacleHandling}(\cdot)$  (line 11) to evaluate traversability. When a feasible expansion node  $n_c$  is generated. The algorithm then attempts to connect  $n_c$  to a downstream key point  $q_m \in \{q_{N_q}, \dots, q_{i+1}\}$  (line 18) to construct a valid path. For example, if a connection is established from  $n_c$  to  $q_{i+2}$ , a forward path  $S_{\text{con}}$  is generated. Subsequently, a backward path  $S_{\text{back}}$  from  $q_i$  to  $n_c$  is constructed (line 20). The resulting segmented path  $S_{\text{seg}}$ , connecting  $q_i$  to  $q_{i+2}$ , is obtained by concatenating  $S_{\text{back}}$  and  $S_{\text{con}}$ . Finally, the algorithm returns  $S_{\text{seg}}$  along with the updated key point index  $m = i + 2$ , as shown in Fig. 8. If no valid downstream connections can be established from  $n_c$  using any motion mode of the 4WIS vehicle, the algorithm continues by expanding a new node  $n_c$  from the current node and repeating the loop (line 9) until either a feasible key point  $q$  is found or the maximum iteration is reached.

**Algorithm 2** Improved4WISHybridAstar**Require:** Current index  $i$ , key point  $q_i$ , key point set  $\mathcal{Q}$ 


---

```

1: Initialize: Open set  $O \leftarrow \emptyset$ , closed set  $C \leftarrow \emptyset$ ,  $j \leftarrow 1$ , cost set  $F \leftarrow \emptyset$ , segment path  $S_{\text{seg}} \leftarrow \emptyset$ 
2: if TrajConnect( $q_i, q_{i+1}$ )  $\neq \emptyset$  then
3:   return TrajConnect( $q_i, q_{i+1}$ ),  $i + 1$ 
4: end if
5: Add  $q_i$  to the open set  $O$ , add  $F(q_i)$  into the cost set  $\mathcal{F}$ 
6: while  $O \neq \emptyset$  and  $j \leq \text{MaxIteration1}$  do
7:    $n_p \leftarrow \text{FindMinCostNode}(O, \mathcal{F})$  ▷  $n_p \in O$  minimum cost
8:   Remove  $n_p$  from open set  $O$  and add to close set  $C$ 
9:   for action  $a$  in the motion sets  $M_s$  do
10:    Expand node  $n_c$  from  $n_p$  with action  $a$  using (1), (2), (3)
11:    if  $n_c \in C$  or ObstacleHandling( $n_c$ ) in (33) is FALSE then
12:      continue ▷ Skip invalid or colliding node
13:    end if
14:    Compute the node cost  $F(n_c)$  using (26)
15:    Add  $n_c$  to open set  $O$ , add  $F(n_c)$  to cost set  $\mathcal{F}$ 
16:    for  $m$  in  $\{N_q, N_q - 1, \dots, i + 1\}$  do
17:      Select  $q_m$  from key points set  $\mathcal{Q}$ 
18:       $S_{\text{con}} \leftarrow \text{TrajConnect}(n_c, q_m)$  ▷ path from  $n_c$  to  $q_m$ 
19:      if  $S_{\text{con}} \neq \emptyset$  then
20:         $S_{\text{back}} \leftarrow \text{BackTracking}(n_c, q_i)$  ▷ Backward path from  $q_i$  to  $n_c$ 
21:         $S_{\text{seg}} \leftarrow S_{\text{back}} + S_{\text{con}}$  ▷ path  $q_i$  to  $q_m$ 
22:        return  $S_{\text{seg}}, m$ 
23:      end if
24:    end for
25:  end for
26:   $j \leftarrow j + 1$ 
27: end while

```

**Ensure:** Segmented path  $S_{\text{seg}}$ , index  $m$ 

## 6. Collision Constraints Formulation

### 6.1. Collision Constraints of Dynamic Obstacles

#### 6.1.1. Probabilistic Risk Field Model

We design a driving risk field model to quantify the driving risks caused by dynamic obstacles with motion uncertainties. This section takes the pedestrian as an example for the risk modeling. There are  $N_p \in \mathbb{Z}^+$  pedestrians in the environment, and the constant acceleration model is used for pedestrians:

$$\begin{cases} x^{p,n}(k+1) = x^{p,n}(k) + v_x^{p,n}(k)\Delta t + \frac{1}{2}a_x^{p,n}(k)\Delta t^2, \\ y^{p,n}(k+1) = y^{p,n}(k) + v_y^{p,n}(k)\Delta t + \frac{1}{2}a_y^{p,n}(k)\Delta t^2, \end{cases} \quad (34)$$

where  $x^{p,n}(k)$  and  $y^{p,n}(k)$  represent the longitudinal and lateral positions of the  $n$ -th ( $n \in [1, N_p]$ ) pedestrians.  $v_x^{p,n}(k)$ ,  $v_y^{p,n}(k)$ ,  $a_x^{p,n}(k)$ ,  $a_y^{p,n}(k)$  denote the longitudinal velocity, lateral velocity, longitudinal acceleration, and lateral acceleration, respectively.  $\Delta t$  is the time interval. Considering motion uncertainties, we define the variances of the pedestrian's position as:

$$\mathbf{D}^{p,n}(k) = \begin{bmatrix} \text{Var}(x^{p,n}(k)) & 0 \\ 0 & \text{Var}(y^{p,n}(k)) \end{bmatrix}, \quad (35)$$

where  $\mathbf{D}^{p,n}(k)$  is the covariance matrix,  $\text{Var}(x^{p,n}(k))$  and  $\text{Var}(y^{p,n}(k))$  are the variances of longitudinal and lateral positions:

$$\begin{cases} \text{Var}(x^{p,n}(k)) = \sigma_x^2 + \sum_{i=1}^k \left( \Delta t^2 (\sigma_{vx}^2 + (\sigma_{ax}^n(i))^2 \Delta t^2) + \frac{(\sigma_{ax}^n(i))^2 \Delta t^4}{4} \right), \\ \text{Var}(y^{p,n}(k)) = \sigma_y^2 + \sum_{i=1}^k \left( \Delta t^2 (\sigma_{vy}^2 + (\sigma_{ay}^n(i))^2 \Delta t^2) + \frac{(\sigma_{ay}^n(i))^2 \Delta t^4}{4} \right), \end{cases} \quad (36)$$

where  $\sigma_x^2$  and  $\sigma_y^2$  are the initial position variances along x-axis and y-axis,  $\sigma_{vx}^2$  and  $\sigma_{vy}^2$  are velocity variances, and  $(\sigma_{ax}^n(i))^2$  and  $(\sigma_{ay}^n(i))^2$  are the acceleration variances at the sampling time  $i$ , respectively.

We construct a continuous risk potential field to quantify collision risk, where the Mahalanobis distance [31] is used to evaluate the standardized spatial relationship between the vehicle and each pedestrian:

$$d_M^n(k) = \sqrt{(\mathbf{r}^n)^\top (\mathbf{D}^{p,n}(k))^{-1} \mathbf{r}^n}, \quad \mathbf{r}^n = \begin{bmatrix} x(k) - x^{p,n}(k) \\ y(k) - y^{p,n}(k) \end{bmatrix}, \quad (37)$$

where  $d_M^n(k)$  denotes the Mahalanobis distance between the vehicle position  $(x(k), y(k))$  and the predicted position of the  $n$ -th pedestrian at time  $k$ . Referring to [32] and [33], the driving risk field model is formulated as:

$$U^{p,n}(k) = \begin{cases} \alpha \left( \frac{1}{d_M^n(k)} - \frac{1}{d_s} \right)^2 \cdot \frac{\mathbf{r}^n(k)}{|\mathbf{r}^n(k)|} \cdot e^{-\beta v_r}, & d_M^n(k) \leq d_s, \\ 0, & d_M^n(k) > d_s, \end{cases} \quad (38)$$

where  $U^{p,n}(k)$  denotes the driving risk field value at time  $k$ ,  $d_s$  is the safety distance,  $\alpha$  and  $\beta$  are the constant coefficients,  $v_r$  is the relative velocity.

The overall instantaneous risk potential field at time  $k$  is then computed by aggregating pedestrians:

$$U^p(k) = \max_{1 \leq n \leq N_p} U^{p,n}(k), \quad (39)$$

where  $U(k)$  represents the maximum potential risk.

### 6.1.2. Collision Constraints with Driving Corridor

Considering motion uncertainties, we construct the driving corridor for dynamic obstacles based on the driving risk field model designed above. The driving corridor is then utilized to formulate the linear constraints within the OCP in (7). The driving corridor of the dynamic obstacle at the sampling point  $(x(j), y(j))$  can be efficiently obtained in the same way as described in Section 2. For each sampling point  $(x(j), y(j))$ , we require that the potential risks within the driving corridor remain below a predefined threshold  $\epsilon_{\text{threshold}}$ . If the driving risk is higher than the safe threshold, we adjust the driving corridor until it satisfies safety requirements.  $\mathcal{E}_j^{\text{up}}$  is the upper boundary of the driving corridor at point  $(x(j), y(j))$ . We set  $M$  sampling points uniformly along the boundary  $\mathcal{E}_j^{\text{up}}$ , and each point is denoted as  $(x_{\mathcal{E}_j^{\text{up}}}^m, y_{\mathcal{E}_j^{\text{up}}}^m)$ ,  $1 \leq m \leq M$  and the driving risk of the position is denoted by  $U_{\mathcal{E}_j^{\text{up}}}^{m,p}$ , which is computed using (39).

When the driving risk exceeds the safety threshold  $\epsilon_{\text{threshold}}$ , the expansion length  $l_j^{\text{up}}$  in the upward direction  $\mathcal{E}_j^{\text{up}}$  is iteratively reduced until the safety condition is met. This adjustment process can be described as follows:

$$l_j^{\text{up}}(z+1) = \begin{cases} l_j^{\text{up}}(z) - \Delta l, & \text{if } U_{\mathcal{E}_j^{\text{up}}}^{m,p} > \epsilon_{\text{threshold}}, \\ l_j^{\text{up}}(z), & \text{otherwise,} \end{cases} \quad (40)$$

where  $l_j^{\text{up}}(z)$  denotes the expansion length in the upward direction at the  $z$ -th iteration,  $\Delta l$  representing the step size. The expansion lengths in the other directions can be computed in a similar manner. Based on this, the safe driving corridor  $\mathcal{C}_j^\epsilon$  centered at the point  $(x(j), y(j))$  can be constructed to ensure that the driving risk remains below the

safety threshold. The corresponding linear collision avoidance constraints based on the safe corridor  $C_j^\epsilon$  can then be formulated as follows:

$$\mathcal{E}_{\epsilon,j}^{\text{left}} \leq x(j) \leq \mathcal{E}_{\epsilon,j}^{\text{right}}, \mathcal{E}_{\epsilon,j}^{\text{down}} \leq y(j) \leq \mathcal{E}_{\epsilon,j}^{\text{up}}, \quad (41)$$

where  $\mathcal{E}_{\epsilon,j}^{\text{left}}$ ,  $\mathcal{E}_{\epsilon,j}^{\text{right}}$ ,  $\mathcal{E}_{\epsilon,j}^{\text{down}}$ , and  $\mathcal{E}_{\epsilon,j}^{\text{up}}$  denote the left, right, lower, and upper boundaries of the safe corridor  $C_j^\epsilon$ , respectively. The collision avoidance constraints are included in the OCP in Section 2. By incorporating the driving risk field model, we aim to improve the robustness of the OCP framework, considering the motion uncertainties caused by dynamic obstacles.

## 6.2. Logical Constraints of Drive-Over Obstacles

As discussed previously, the “drive-over” obstacles, such as puddles, speed bumps, and cardboard boxes, can be driven over at low speeds. To enforce appropriate speed constraints when navigating these obstacles, we introduce logical constraints within the OCP framework in (7):

$$\chi_{\text{area}}(x(j), y(j)) \times \zeta(v(j)) = 0, j = 0, 1, 2, \dots, N_f, \quad (42)$$

where  $x(j)$  and  $y(j)$  are the vehicle’s position at the  $j$ -th sample point along its trajectory, the function  $\chi_{\text{area}}(x(j), y(j))$  serves as an indicator, returning 1 if the vehicle is driving through “drive-over” obstacle region and 0 otherwise.  $\zeta(v(j))$  is the constraint on the vehicle’s velocity. Notably, the constraint in (42) is activated only when  $\chi_{\text{area}}(x(j), y(j)) = 1$ , *i.e.*, when the vehicle is traversing the “drive-over” obstacles. The indicator function  $\chi_{\text{area}}(x(j), y(j))$  is formulated as:

$$\chi_{\text{area}}(x(j), y(j)) = \begin{cases} 1, & \text{if } x(j) \in [x_o^l, x_o^u], y(j) \in [y_o^l, y_o^u], \\ 0, & \text{otherwise,} \end{cases} \quad (43)$$

where  $x_o^l, x_o^u$  are the lower and upper bounds of the obstacle region along the x-axis, and  $y_o^l, y_o^u$  are the corresponding bounds along the y-axis.  $x(j) \in [x_o^l, x_o^u], y(j) \in [y_o^l, y_o^u]$ , indicates that the vehicle’s current position lies within the specified obstacle region. The vehicle’s speed constraint  $\zeta(v(j))$  is formulated as:

$$\zeta(v(j)) = \max \{0, \max (v(j) - v_{\text{ub}}, v_{\text{lb}} - v(j))\}, \quad (44)$$

where  $v_{\text{lb}}$  and  $v_{\text{ub}}$  are the lower bound and upper bound of the allowable speed range. This function evaluates to zero when the vehicle’s speed  $v(j)$  is within the permissible range  $[v_{\text{lb}}, v_{\text{ub}}]$  and yields a positive value proportional to the extent of the violation otherwise. This expression enforces that the vehicle’s speed lies within the allowable interval  $[v_{\text{lb}}, v_{\text{ub}}]$  while navigating through the region of “drive-over” obstacles. By integrating the logical constraints (42) into the OCP in (7), we ensure that the vehicle maintains appropriate speeds when traversing “drive-over” obstacles, thereby enhancing safety and compliance with operational guidelines.

## 7. Experiment Results

To assess the performance of the proposed methods across varying levels of scenario complexity, we construct a series of test scenarios categorized by obstacle density: low (5 obstacles), medium (7 obstacles), and high (9 obstacles). Each category encompasses 50 distinct scenarios, and there are 150 test scenarios for evaluation. The detailed configurations, along with the training procedures and corresponding results of the neural network, are comprehensively presented in Appendix A.

### 7.1. Comparative Study

This section evaluates the effectiveness of the proposed trajectory planning framework for 4WIS vehicles. A total of 150 scenarios that can be solved by the hybrid A\* algorithm are selected, where randomly placed “crossable” and “drive-over” obstacles of varying shapes and sizes are introduced along the hybrid A\* path to increase task complexity. Additionally, dynamic obstacles are randomly included. The trajectory performances of our method are compared against two baseline methods, *i.e.*, Hybrid A\* [15] and FTHA [16], as summarized in Table 1. Our method consistently outperforms both baselines across all metrics. It achieves the highest success rate of 85.33%, significantly exceeding that of hybrid A\* (55.33%) and FTHA (70.67%). It also produces the shortest path length (36.121 m) and traversal

**Table 1**

Comparison of planning results of our method (full model) and two baseline methods regarding 150 scenarios.

Method	Success Rate (%) ↑	Path Length (m) ↓	Traversal Time (s) ↓	Maximum Jerk (m/s <sup>3</sup> ) ↓	Average Jerk (m/s <sup>3</sup> ) ↓	Computation Time (s) ↓	Cumulative Risk Potential ↓
Hybrid A*	55.33	36.623	33.503	0.474	0.364	40.817	7.590
FTHA	70.67	36.223	33.123	0.437	0.318	42.731	7.284
<b>Ours (Full)</b>	<b>85.33</b>	<b>36.121</b>	<b>32.545</b>	<b>0.408</b>	<b>0.278</b>	<b>26.803</b>	<b>4.119</b>

Note: All initial paths are assumed to be subsequently optimized by solving the optimal control problem to obtain the final trajectory.

**Table 2**

Ablation study: comparative results of 4WIS Hybrid A\* with/without GP.

Method	Success Rate (%) ↑	Path Length (m) ↓	Traversal Time (s) ↓	Computation Time (s) ↓	Maximum Jerk (m/s <sup>3</sup> ) ↓	Average Jerk (m/s <sup>3</sup> ) ↓
4WIS Hybrid A*	80%	29.482	41.845	35.630	0.495	0.332
<b>4WIS Hybrid A*+GP</b>	<b>90%</b>	<b>21.570</b>	<b>36.593</b>	<b>25.487</b>	<b>0.433</b>	<b>0.236</b>

Note: all methods generate initial paths, and then are optimized by OCP.

**Table 3**

Ablation study: comparative results of 4WIS Hybrid A\*+GP with/without MCN.

Method	Computation Time (s) ↓
4WIS Hybrid A*+GP	46.848
<b>4WIS Hybrid A*+MCN+GP</b>	<b>38.166</b>

Note: all methods generate initial paths, and then are optimized by OCP.

time (32.545 s), demonstrating superior path efficiency. In terms of motion smoothness, our method achieves the lowest maximum jerk (0.408 m/s<sup>3</sup>) and average jerk (0.278 m/s<sup>3</sup>), enabling safer and more comfortable maneuvers. Moreover, our method has achieved the shortest computation time (26.803 s), indicating the superior computational efficiency. Notably, our method reduces the cumulative risk potential to 4.119, significantly lower than hybrid A\* (7.590) and FTHA (7.284), highlighting its enhanced safety in dynamic and cluttered environments.

## 7.2. Validation of Multimodal Classification Network and Guided Points

### 7.2.1. Guided Points

We first evaluate the effectiveness of the guided point in our method. We compare the trajectory performance of the 4WIS hybrid A\* algorithm with and without the guided point using 50 randomly selected planning tasks, as shown in Table 2, which demonstrates the effectiveness of guided points in trajectory planning. With guided points, our method demonstrates a notable performance improvement, achieving a higher success rate (90% vs. 80%), while significantly reducing the path length (from 29.482 m to 21.570 m) and traversal time (from 41.845 s to 36.593 s). Additionally, the computation time has been reduced by more than 10 seconds. The generated trajectories are also smoother, as evidenced by the reductions in maximum jerk (0.433 m/s<sup>3</sup> vs. 0.495 m/s<sup>3</sup>) and average jerk (0.236 m/s<sup>3</sup> vs. 0.332 m/s<sup>3</sup>). These results show the effectiveness of guided points in improving travel efficiency, smoothness of the trajectories, and computational efficiency.

### 7.2.2. Multimodal Classification Network

The multimodal classification network is expected to improve computational efficiency, and we evaluate the computation time of the 4WIS hybrid A\* algorithm with and without the multimodal classification network using 50 randomly selected planning tasks, as shown in Table 3. With the multimodal classification network, the computation time decreases from 46.848 s to 38.166 s, resulting in an approximate 18.5% improvement in computational efficiency, showing the effectiveness of this module.

**Table 4**

Ablation study: comparison of trajectory planning results of 4WIS Hybrid A\*+MCN+GP with two baseline methods.

	Method	Success Rate (%) $\uparrow$	Path Length (m) $\downarrow$	Traversal Time (s) $\downarrow$	Maximum Jerk (m/s <sup>3</sup> ) $\downarrow$	Average Jerk (m/s <sup>3</sup> ) $\downarrow$	Computation Time (s) $\downarrow$
Low Density	Hybrid A*	96%	<b>25.324</b>	<b>17.798</b>	0.851	0.389	<b>9.727</b>
	FTHA	100%	29.003	30.806	0.817	0.318	20.646
	<b>4WIS Hybrid A*+MCN+GP</b>	<b>100%</b>	26.155	18.292	<b>0.766</b>	<b>0.302</b>	9.945
Medium Density	Hybrid A*	42%	64.934	40.314	0.475	0.292	122.470
	FTHA	64%	66.558	51.843	0.568	0.285	122.124
	<b>4WIS Hybrid A*+MCN+GP</b>	<b>84%</b>	<b>47.975</b>	<b>30.323</b>	<b>0.308</b>	<b>0.168</b>	<b>34.481</b>
High Density	Hybrid A*	38%	60.048	69.117	0.483	0.288	87.607
	FTHA	68%	55.354	38.470	0.745	0.306	75.338
	<b>4WIS Hybrid A*+MCN+GP</b>	<b>82%</b>	<b>45.499</b>	<b>35.965</b>	<b>0.453</b>	<b>0.192</b>	<b>23.156</b>

Note: All methods generate initial paths and are optimized by OCP.

### 7.2.3. Multimodal Classification Network and Guided Points

This section validates the effectiveness of the integration of the multimodal classification network and the guided points, and chooses hybrid A\* [15] and FTHA [16] as baseline methods. The experiments are conducted across three obstacle density levels: low, medium, and high, as summarized in Table 4. Our method consistently outperforms both baselines across all metrics in medium and high density scenarios. Considering the success rate, our method consistently outperforms hybrid A\* and FTHA in terms of the success rate metric across all obstacle densities. Specifically, it achieves a 100% success rate in low-density environments and significantly higher success rates in medium (84%) and high density (82%) scenarios compared to hybrid A\* (42%, 38%) and FTHA (64%, 68%). Regarding path length and traversal time, our method demonstrates superior performance in medium and high-density settings. While hybrid A\* shows advantages in travel efficiency in low-density environments, our method achieves comparable performance, indicating its path efficiency. Additionally, our approach ensures the smoothest trajectories, exhibiting the lowest maximum and average jerk values across all environments. In terms of computation time, our method achieves the minimum in medium and high-density scenarios (34.481 s and 23.156 s, respectively) and maintains comparable efficiency to hybrid A\* in low-density scenarios (9.727 s vs. 9.945 s). Fig. 9 demonstrates that all methods can generate feasible trajectories in low-density scenarios, with our approach achieving computation times comparable to hybrid A\*. In medium-density environments, hybrid A\* fails to produce feasible paths, while FTHA can find a path but requires significantly more computation time. In high-density scenarios, FTHA’s optimization process fails due to violations of the vehicle’s kinematic constraints. In contrast, our method consistently generates high-quality initial paths that adhere to kinematic constraints, ensuring successful optimization across all obstacle densities.

## 7.3. Validation of Hierarchical Obstacle Handling Strategy

### 7.3.1. Crossable Obstacle

The effectiveness of the “Crossable” Obstacle Handling Strategy (COHS) is evaluated. We selected 50 scenarios that can be solved by the 4WIS hybrid A\* algorithm and introduced randomly placed “crossable” obstacles of varying shapes and sizes along the 4WIS hybrid A\* path to increase task complexity. We then compared the trajectory performance of the 4WIS hybrid A\* algorithm with and without the proposed “crossable” obstacle handling strategy, as summarized in Table 5. The proposed method achieves a success rate of 92%, significantly higher than the 70% of 4WIS hybrid A\*. It also outperforms 4WIS hybrid A\* in terms of path length (26.872 m vs. 28.325 m) and traversal time (22.860 s vs. 23.219 s), indicating improved path efficiency. Furthermore, it yields lower maximum jerk (0.498 m/s<sup>3</sup>) and average jerk (0.348 m/s<sup>3</sup>), resulting in smoother and more comfortable trajectories. Although it incurs a slight increase in computation time, the proposed method demonstrates substantial improvements in success rate, path efficiency, and path smoothness. Fig. 10 illustrates two examples of the trajectory planning results for 4WIS hybrid A\* and the proposed method in environments containing “crossable” obstacles. In Case 1, 4WIS hybrid A\* conservatively avoids all obstacles, including “crossable” ones, resulting in a longer path (42.82 m) and higher computation time (32.204 s). In contrast, the proposed method efficiently navigates narrow regions by traversing the “crossable” obstacles, producing a shorter path (26.63 m) with reduced computation time (14.064 s). In Case 2, 4WIS hybrid A\* fails to generate a valid initial trajectory, while the proposed method successfully computes a feasible and optimized path by exploiting obstacle traversability. These results highlight the proposed method’s superior adaptability and efficiency in constrained environments with “crossable” obstacles.

**Table 5**

Comparison of planning results of 4WIS Hybrid A\* with and without Crossable Obstacle Handling Strategy (COHS).

Method	Success Rate (%)	Path Length (m)	Traversal Time (s)	Computation Time (s)	Maximum Jerk (m/s <sup>3</sup> )	Average Jerk (m/s <sup>3</sup> )
4WIS Hybrid A*+COHS	<b>92%</b>	<b>26.872</b>	<b>22.860</b>	17.603	<b>0.498</b>	<b>0.348</b>
4WIS Hybrid A*	70%	28.325	23.219	<b>15.844</b>	0.527	0.355

Note: all methods listed above are used to generate the initial path, and then optimized by OCP.

**Table 6**

Comparison of planning results using 4WIS Hybrid A\* with and without Drive-Over Obstacle Handling Strategy (DOHS).

Method	Success Rate (%)	Path Length (m)	Traversal Time (s)	Computation Time (s)	Maximum Jerk (m/s <sup>3</sup> )	Average Jerk (m/s <sup>3</sup> )
4WIS Hybrid A* + DOHS	<b>90</b>	<b>23.420</b>	<b>24.579</b>	22.827	0.517	<b>0.361</b>
4WIS Hybrid A*	76	27.242	25.921	<b>20.968</b>	<b>0.498</b>	0.375

Note: DOHS impacts the node expansion of 4WIS Hybrid A\* and velocity optimization in OCP.

**Table 7**

Comparison of planning results using 4WIS Hybrid A\* with and without the Risk Field-based Driving Corridor (RFDC).

Method	Cumulative Risk Potential ↓	Minimum Distance (m) ↑	Path Length (m) ↓	Traversal Time (s) ↓	Computation Time (s) ↓
4WIS Hybrid A* + RFDC	<b>3.235</b>	<b>1.591</b>	35.472	25.383	21.177
4WIS Hybrid A*	10.141	0.884	<b>33.414</b>	<b>24.623</b>	<b>22.552</b>

Note: 4WIS Hybrid A\* generates initial paths. RFDC generates collision constraints of dynamic obstacles in OCP.

### 7.3.2. Drive-Over Obstacle

The “Drive-over” Obstacles Handling Strategy (DOHS) enables the vehicle to safely traverse low-profile obstacles at low speeds. To evaluate its effectiveness, we selected 50 scenarios that can be solved by the 4WIS hybrid A\* algorithm and randomly placed “drive-over” obstacles of varying shapes and sizes along the 4WIS hybrid A\* path to increase task complexity. We then compared the trajectory performance of the 4WIS hybrid A\* algorithm with and without the proposed “drive-over” obstacle handling strategy, as summarized in Table 6. The proposed method achieves a success rate of 90%, significantly higher than the 76% of 4WIS hybrid A\*. It also outperforms in path length (23.420 m vs. 27.242 m) and traversal time (24.579 s vs. 25.921 s), demonstrating enhanced path efficiency. In addition, the proposed approach yields a lower average jerk (0.361 m/s<sup>3</sup> vs. 0.375 m/s<sup>3</sup>) and a comparable maximum jerk (0.517 m/s<sup>3</sup> vs. 0.498 m/s<sup>3</sup>), indicating improved trajectory smoothness. While the computation time increases slightly, the strategy delivers notable gains in success rate, path efficiency, and trajectory quality. Fig. 11 illustrates the trajectory planning results of the 4WIS hybrid A\* algorithm and our method in narrow environments containing “drive-over” obstacles. In Case 1, the 4WIS hybrid A\* algorithm detours around each obstacle, while our method chooses to safely drive over the obstacles, reducing the path length by approximately 4 m. Case 2 illustrates a more challenging scenario in which the 4WIS hybrid A\* fails to generate a feasible path, whereas our approach successfully yields an optimal trajectory. These results demonstrate that the “drive-over” obstacle-handling strategy in our method can enhance path efficiency. Furthermore, the velocity and acceleration of Case 2 are illustrated in Fig. 12. The vehicle decelerates and then proceeds at a constant speed of 2.0 m/s with zero acceleration when passing over the “drive-over” obstacle, thereby ensuring safe traversal.

### 7.4. Impact of Driving Risk Field-based Driving Corridor

To evaluate the effectiveness of probabilistic risk field-based driving corridors in trajectory planning, we compared the performance of the 4WIS hybrid A\* algorithm with and without this safety mechanism. Additionally, we calculated the cumulative risk potentials to assess the safety performance of both methods. As shown in Table 7, our approach yields a cumulative risk potential of 3.235, significantly lower than the 10.141 observed for 4WIS hybrid A\*. Furthermore, the minimum distance to obstacles achieved by our method is 1.591 m, notably greater than the 0.884 m

of 4WIS hybrid A\*, indicating enhanced safety. These results demonstrate that incorporating a probabilistic risk field-based driving corridor significantly improves safety while maintaining comparable efficiency. Although our method results in a slightly longer path and increased traversal time, it achieves improved safety.

## 8. Conclusion

This study proposes an efficient trajectory planning framework for 4WIS vehicles in narrow and dynamic environments. The method first employs a multimodal classification network to assess scene complexity and set guided points to decompose complex tasks into simple ones, thereby enhancing search efficiency. The node cost and mode-switching penalties are designed for 4WIS vehicles to fully exploit their motion capabilities and reduce unnecessary reversals and frequent mode switches. To further improve path efficiency in constrained environments, we introduce a hierarchical obstacle handling strategy that guides the node expansion of the 4WIS hybrid A\* based on obstacle attributes. A velocity constraint is also imposed when handling “drive-over” obstacles to ensure safe traversal. Moreover, considering dynamic obstacles with motion uncertainty, we propose a probabilistic risk field-based corridor generation method, which formulates linear safety constraints to reduce computational complexity. Experimental results validate the effectiveness of our method in achieving safe, efficient trajectory planning for 4WIS vehicles. Future work will explore learning-based approaches to further enhance adaptability to complex environments.

## References

- [1] Yang, J., Wang, J., Li, J., Meng, X., Jiang, X., Lu, C., 2025. Sobol sequence rrt\* and numerical optimal joint algorithm-based automatic parking trajectory planning of four-wheel steering vehicles. *Rob. Auton. Syst.* 186, 104909.
- [2] Chang, Y., Yang, Z., Hu, M., Bian, Y., Li, Y., 2024. An optimal parking path planning method integrating motion mode decision-making for 4wis vehicles, in: *IEEE Int. Conf. Intell. Transp. Syst. (ITSC)*, pp. 2570–2577.
- [3] Guo, Y., Guo, Z., Wang, Y., Yao, D., Li, B., Li, L., 2023. A survey of trajectory planning methods for autonomous driving — part i: Unstructured scenarios. *IEEE Trans. Intell. Veh.* , 1–29.
- [4] Guo, Y., Yao, D., Li, B., Gao, H., Li, L., 2022. Down-sized initialization for optimization-based unstructured trajectory planning by only optimizing critical variables. *IEEE Trans. Intell. Veh.* 8, 709–720.
- [5] Zhang, H., Zhang, Y., Liu, C., Zhang, Z., 2023. Energy efficient path planning for autonomous ground vehicles with ackermann steering. *Rob. Auton. Syst.* 162, 104366.
- [6] Guo, K., Wang, D., Fan, T., Pan, J., 2021. Vr-orca: Variable responsibility optimal reciprocal collision avoidance. *IEEE Rob. Autom. Lett.* 6, 4520–4527.
- [7] Nagahama, A., Saito, T., Wada, T., Sonoda, K., 2020. Autonomous driving learning preference of collision avoidance maneuvers. *IEEE Trans. Intell. Transp. Syst.* 22, 5624–5634.
- [8] Liu, X., Wang, W., Li, X., Liu, F., He, Z., Yao, Y., Ruan, H., Zhang, T., 2022. Mpc-based high-speed trajectory tracking for 4wis robot. *ISA Trans.* 123, 413–424.
- [9] Yoon, S., Shim, D.H., 2015. Slpa \*: Shape-aware lifelong planning a \* for differential wheeled vehicles. *IEEE Trans. Intell. Transp. Syst.* 16, 730–740.
- [10] Lian, J., Ren, W., Yang, D., Li, L., Yu, F., 2023. Trajectory planning for autonomous valet parking in narrow environments with enhanced hybrid a\* search and nonlinear optimization. *IEEE Trans. Intell. Veh.* 8, 3723–3734.
- [11] Liu, Y., Pei, X., Zhou, H., Guo, X., 2024. Spatiotemporal trajectory planning for autonomous vehicle based on reachable set and iterative lqr. *IEEE Trans. Veh. Technol.* 73, 10932–10947.
- [12] Xu, W., Pan, J., Wei, J., Dolan, J.M., 2014. Motion planning under uncertainty for on-road autonomous driving, in: *IEEE Int. Conf. Robot. Autom. (ICRA)*, pp. 2507–2512.
- [13] Li, S., Wang, W., Wang, B., Guan, H., Liu, H., Wu, S., Chen, H., 2024. Hierarchical trajectory planning based on adaptive motion primitives and bilevel corridor. *IEEE Trans. Veh. Technol.* 73, 16238–16253.
- [14] Ji, Y., Liu, Y., Xie, G., Ma, B., Xie, Z., Cao, B., 2025. Nnpp: A learning-based heuristic model for accelerating optimal path planning on uneven terrain. *Rob. Auton. Syst.* 193, 105084.
- [15] Dolgov, D., Thrun, S., Montemerlo, M., Diebel, J., 2010. Path planning for autonomous vehicles in unknown semi-structured environments. *Int. J. Rob. Res.* 29, 485–501.
- [16] Li, B., Acarman, T., Zhang, Y., Ouyang, Y., Yaman, C., Kong, Q., Zhong, X., Peng, X., 2021. Optimization-based trajectory planning for autonomous parking with irregularly placed obstacles: A lightweight iterative framework. *IEEE Trans. Intell. Transp. Syst.* 23, 11970–11981.
- [17] Allus, A., Unel, M., 2025. Angle-based multi-goal ordering and path-planning using an improved a-star algorithm. *Rob. Auton. Syst.* 190, 105001.
- [18] Teng, J., Li, Y., Yang, Z., Yang, Z., Shao, X., Qin, H., 2024. User preference-aware and efficient trajectory planning for autonomous parking with hybrid a\* and nonlinear optimization, in: *IEEE Int. Conf. Intell. Transp. Syst. (ITSC)*, pp. 1090–1097.
- [19] Liu, C., Lin, C.Y., Tomizuka, M., 2018. The convex feasible set algorithm for real time optimization in motion planning. *SIAM J. Control Optim.* 56, 2712–2733.
- [20] Guo, Y., Yao, D., Li, B., He, Z., Gao, H., Li, L., 2022. Trajectory planning for an autonomous vehicle in spatially constrained environments. *IEEE Trans. Intell. Transp. Syst.* 23, 18326–18336.

- [21] Li, Z., Xie, L., Hu, C., Su, H., 2024. A rapid iterative trajectory planning method for automated parking through differential flatness. *Rob. Auton. Syst.* 182, 104816.
- [22] Li, B., Ouyang, Y., Li, X., Cao, D., Zhang, T., Wang, Y., 2022. Mixed-integer and conditional trajectory planning for an autonomous mining truck in loading/dumping scenarios: A global optimization approach. *IEEE Trans. Intell. Veh.* 8, 1512–1522.
- [23] Xu, F., Liu, X., Chen, W., Zhou, C., 2019. Dynamic switch control of steering modes for four wheel independent steering rescue vehicle. *IEEE Access* 7, 135595–135605.
- [24] Wang, D., Qi, F., 2001. Trajectory planning for a four-wheel-steering vehicle, in: *IEEE Int Conf Rob Autom*, pp. 3320–3325 vol.4.
- [25] Hang, P., Han, Y., Chen, X., Zhang, B., 2018. Design of an active collision avoidance system for a 4wis-4wid electric vehicle. *IFAC-PapersOnLine* 51, 771–777.
- [26] Hua, B., Chai, R., Wang, X., Chai, S., Zhang, J., Xia, Y., 2024. A lightweight optimal trajectory planning for smart summon in highly complex and irregular parking lot scenarios. *IEEE Trans. Intell. Transp. Syst.* 25, 9192–9203.
- [27] Yang, L., Wang, Q., Tan, Y., Gong, J., 2019. Autonomous vehicle path planning considering dwarf or negative obstacles, in: *IEEE 30th Intell. Veh. Symp.*, pp. 1021–1026.
- [28] Park, C., Park, J.S., Manocha, D., 2018. Fast and bounded probabilistic collision detection for high-dof trajectory planning in dynamic environments. *IEEE Trans. Autom. Sci. Eng.* 15, 980–991.
- [29] Wang, M., Zhang, L., Zhang, Z., Wang, Z., 2022. A hybrid trajectory planning strategy for intelligent vehicles in on-road dynamic scenarios. *IEEE Trans. Veh. Technol.* 72, 2832–2847.
- [30] He, K., Zhang, X., Ren, S., Sun, J., 2016. Deep residual learning for image recognition, in: *IEEE/CVF Conf. Comput. Vis. Pattern Recognit*, pp. 770–778.
- [31] Washizawa, Y., Hotta, S., 2014. Mahalanobis distance on extended grassmann manifolds for variational pattern analysis. *IEEE Trans. Neural Networks Learn. Syst.* 25, 1980–1990.
- [32] Jianqiang Wang, Jian Wu, Y.L., 2015. The driving safety field based on driver–vehicle–road interactions. *IEEE Trans. Intell. Transp. Syst.* 16, 2203 – 2214.
- [33] Li, L., Gan, J., Ji, X., Qu, X., Ran, B., 2020. Dynamic driving risk potential field model under the connected and automated vehicles environment and its application in car-following modeling. *IEEE Trans. Intell. Transp. Syst.* 23, 1524–9050.

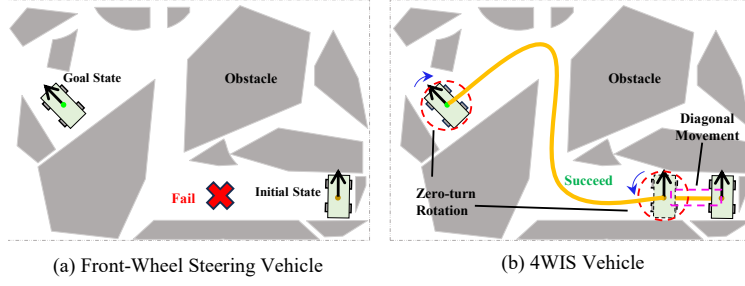


**Figure 1:** Trajectory planning of the front-wheel steering vehicle and the 4WIS vehicle. In contrast, the 4WIS vehicle successfully navigates the narrow space by leveraging multiple motion capabilities.

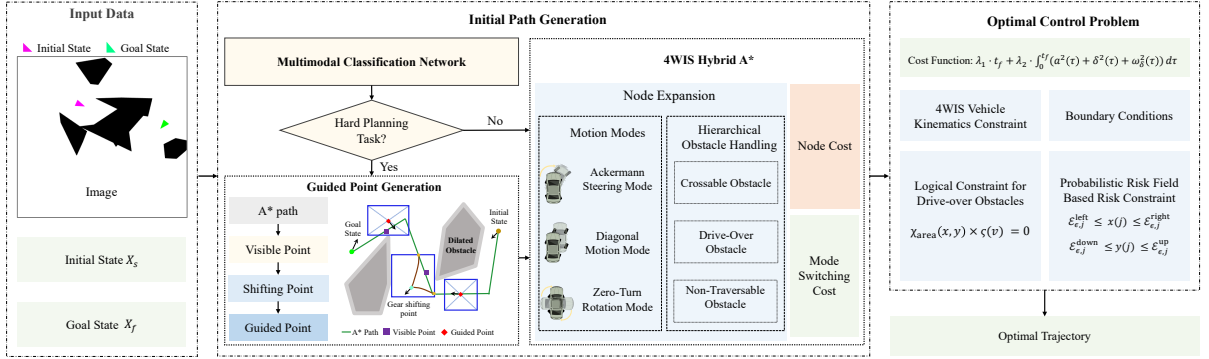


**Figure 2:** Overview of the framework. We use image and vehicle state as inputs, and employ a multimodal classification network to assess the complexity of the planning task. For hard tasks, a guided point generation strategy is activated to facilitate the 4WIS hybrid A\* path planning, which accommodates multiple motion modes and incorporates hierarchical obstacle handling strategies. The 4WIS hybrid A\* initial path is a warm start for solving the OCP.

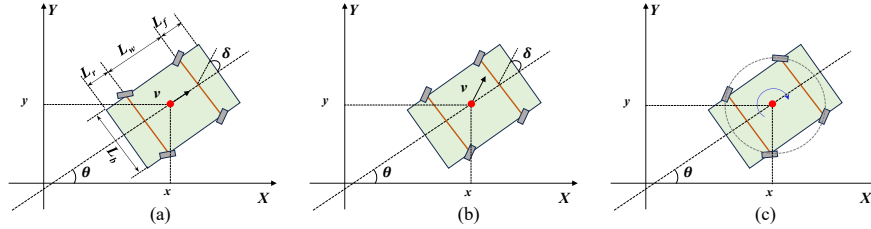


**Figure 3:** 4WIS motion modes. (a) Ackermann steering mode; (b) Diagonal movement mode; (c) Zero-turn rotation mode.

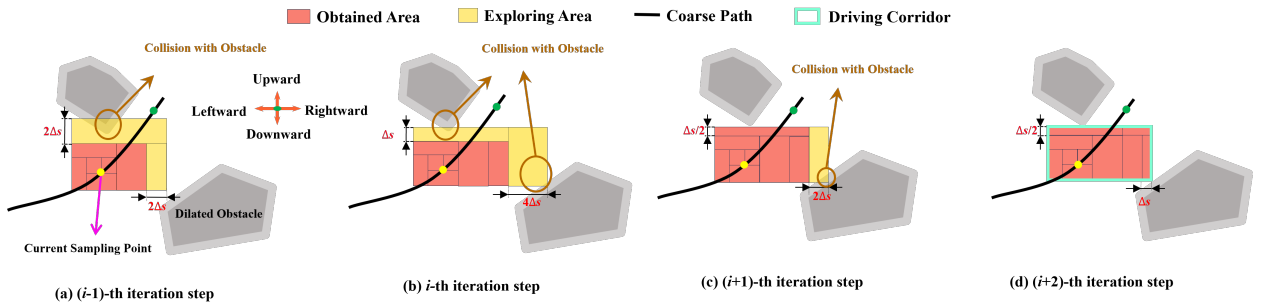


**Figure 4:** Adaptive step size strategy for driving corridor generation. In the  $(i - 1)$  th iteration step, the step size is  $2\Delta s$  in the rightward and upward direction. A collision encountered in the upward direction triggers a reduction in step size, which continues until a collision-free expansion is achieved. Conversely, in the rightward direction, the step size increases iteratively until a collision is detected, after which it is reduced to enable further exploration. The generated driving corridor is shown in (d) after successful expansion.

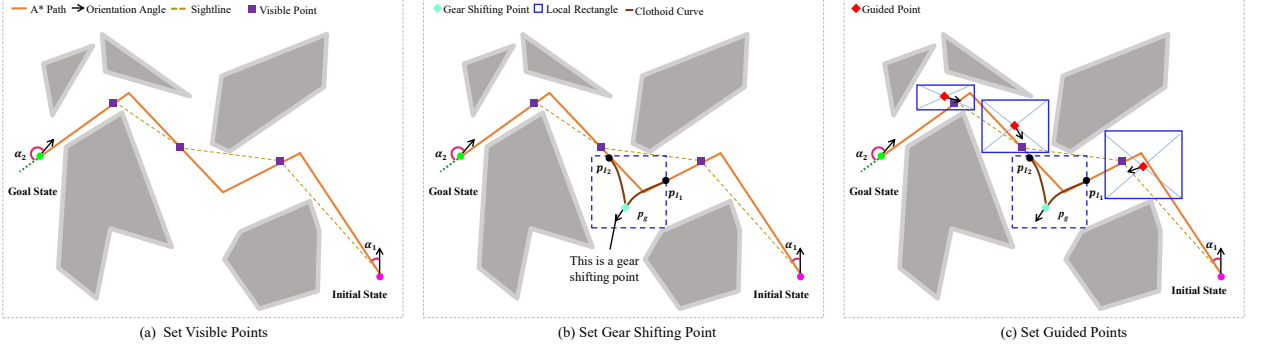


Figure 5: Guided points setting. (a) Visible points. (b) Gear shifting points.

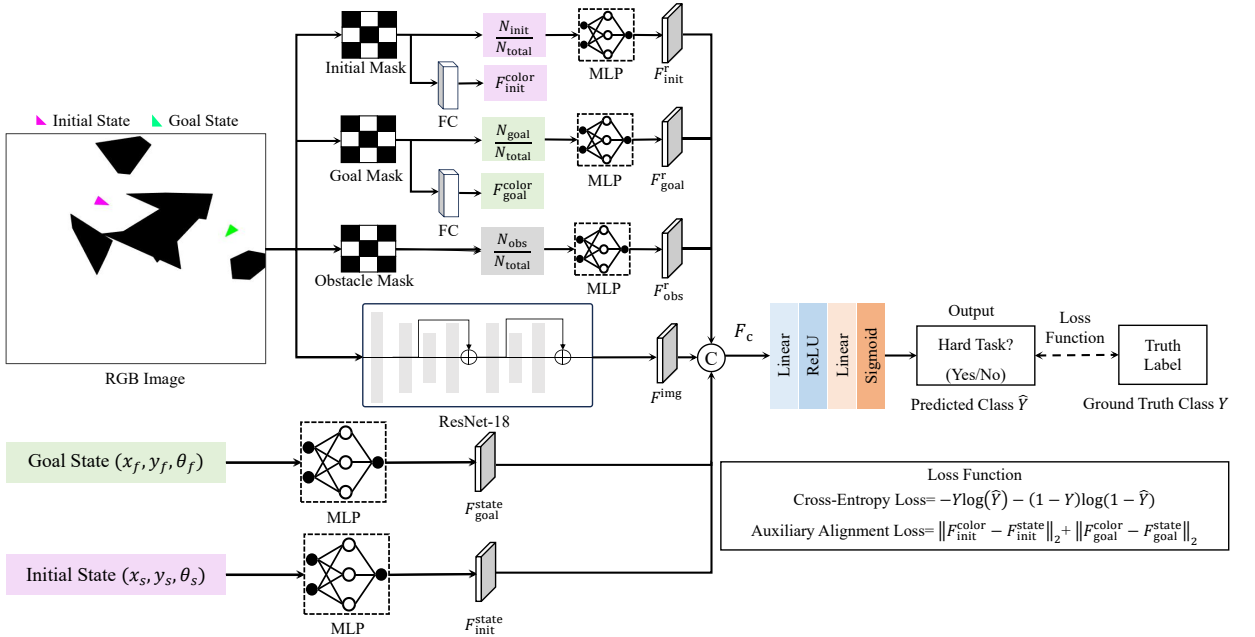


Figure 6: Overview of the multimodal classification network. Semantic masks for the initial region, goal region, and obstacles are generated from the RGB image to capture spatial distributions. A ResNet-18 extracts visual features  $F^{img}$ , while multiple MLPs encode the vehicle's initial and goal states  $F^{state}_{init}$ ,  $F^{state}_{goal}$  and region-based color features  $F^{color}_{init}$ ,  $F^{color}_{goal}$ ,  $F^{color}_{obs}$ . Here,  $N_{init}/N_{total}$ ,  $N_{goal}/N_{total}$ ,  $N_{obs}/N_{total}$  represent the proportion of pixels belonging to the initial, goal, and obstacle regions, respectively. All features are concatenated into a combined vector  $F_c$ , which is passed through fully connected layers to classify whether the planning task is considered hard. An auxiliary alignment loss encourages consistency between the color-derived and state-derived features, enhancing the alignment across modalities.

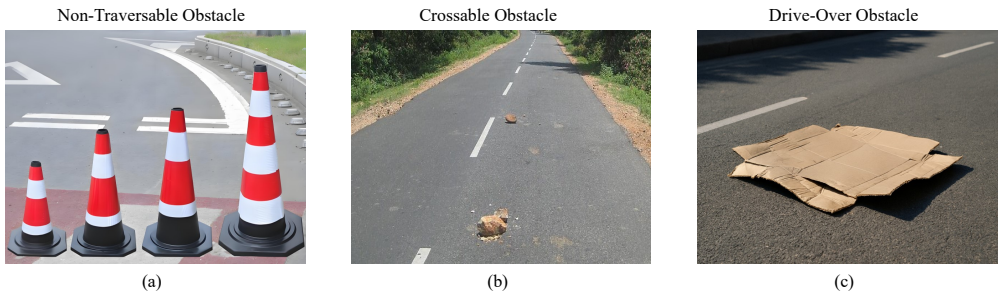
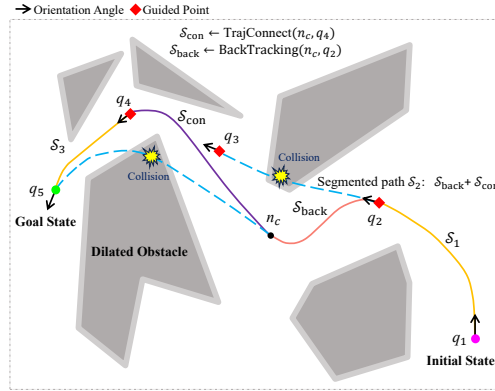
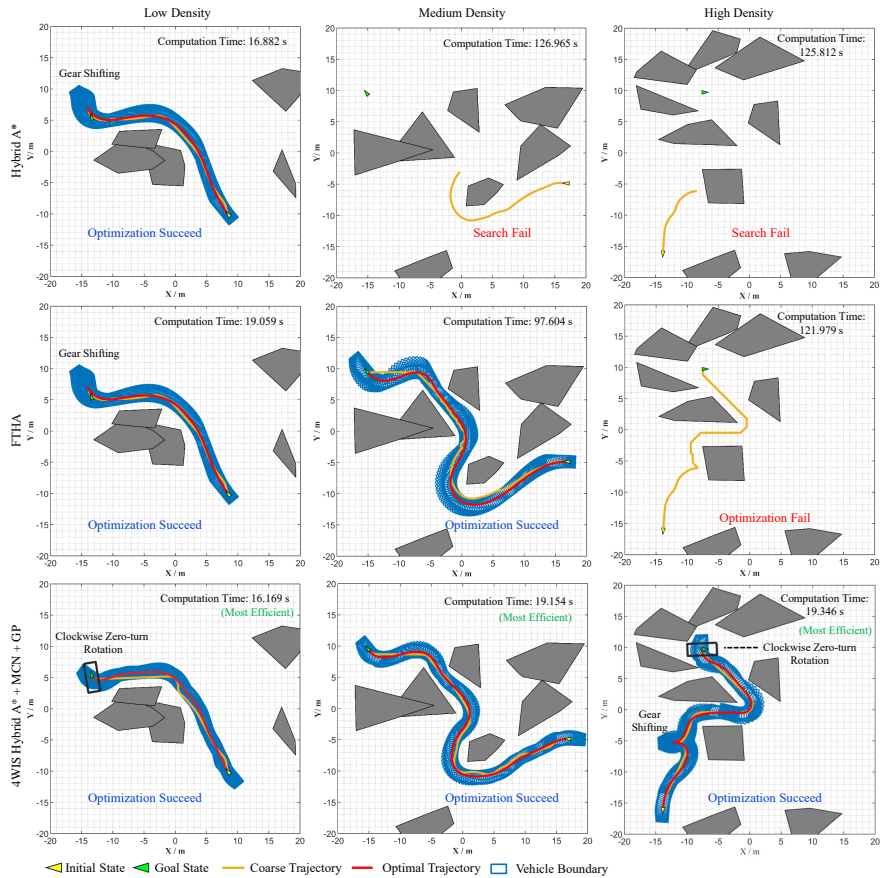


Figure 7: Three types of obstacles. (a) Traffic cones, representing “non-traversable” obstacle; (b) Stones, representing “crossable” obstacle; (c) Cardboard, representing “drive-over” obstacle.



**Figure 8:** Initial path generation. It first establishes a successful direct connection from  $q_1$  to  $q_2$ . It then attempts to connect  $q_2$  to  $q_3$ , but this is found to be infeasible due to collisions. To address this, a node  $n_c$  is expanded from  $q_2$ , and a connection to  $q_5$  is attempted; however, this path fails. It then tries connecting  $n_c$  to  $q_4$ , which results in a feasible forward path, denoted as  $S_{con}$ . A backward path  $S_{back}$  from  $q_2$  to  $n_c$  is subsequently constructed. By concatenating  $S_{back}$  and  $S_{con}$ , the trajectory segment  $S_2$ , connecting  $q_2$  to  $q_4$ , is obtained. In the next iteration, node expansion continues from  $q_4$ , and a direct connection to the goal node  $q_5$  successfully generates the segment  $S_3$ . Finally, the segments  $S_1$ ,  $S_2$ , and  $S_3$  are concatenated to construct the complete initial path.



**Figure 9:** Visualization of the 4WIS hybrid A\* algorithm with a Multimodal Classification Network (MCN) and Guided Points (GP). The hybrid A\* algorithm (top row) succeeds only in low-density environments and fails as obstacle density increases. The FTHA method (middle row) generates optimized trajectories under low and medium densities but fails to optimize under high-density obstacle scenarios. In contrast, 4WIS hybrid A\* with MCN and GP consistently generates feasible trajectories across all density levels. These results highlight the effectiveness of the proposed MCN and GP.

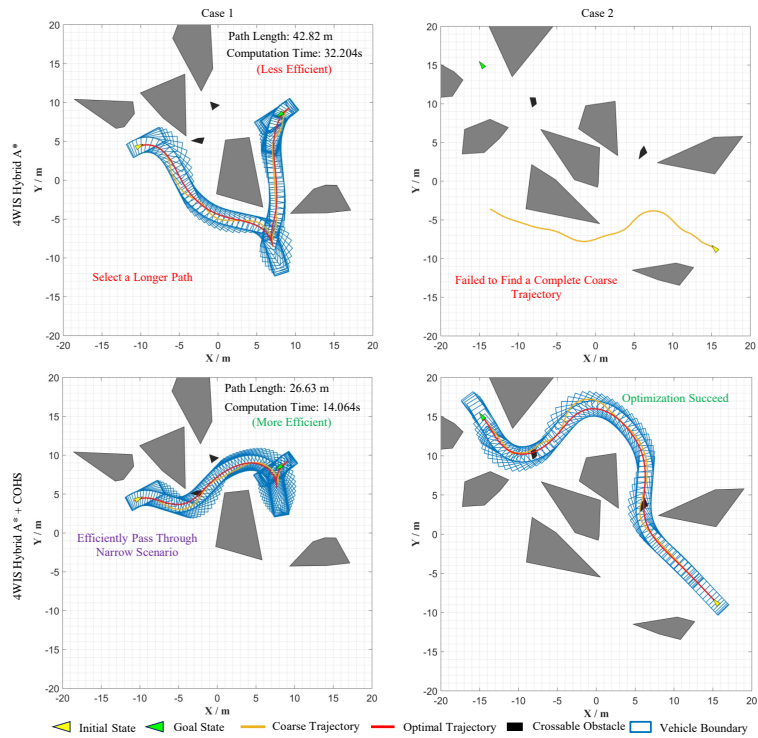


**Figure 10:** Visualization of the 4WIS hybrid A\* algorithm with and without the "crossable" obstacle handling strategy. In the top row, the 4WIS hybrid A\* avoids all obstacles, leading to a longer path in Case 1 and failing to generate a valid path in Case 2. In contrast, the 4WIS hybrid A\* algorithm with the crossable obstacle handling strategy (COHS) generates shorter and feasible paths in both cases, demonstrating enhanced path efficiency in constrained environments.

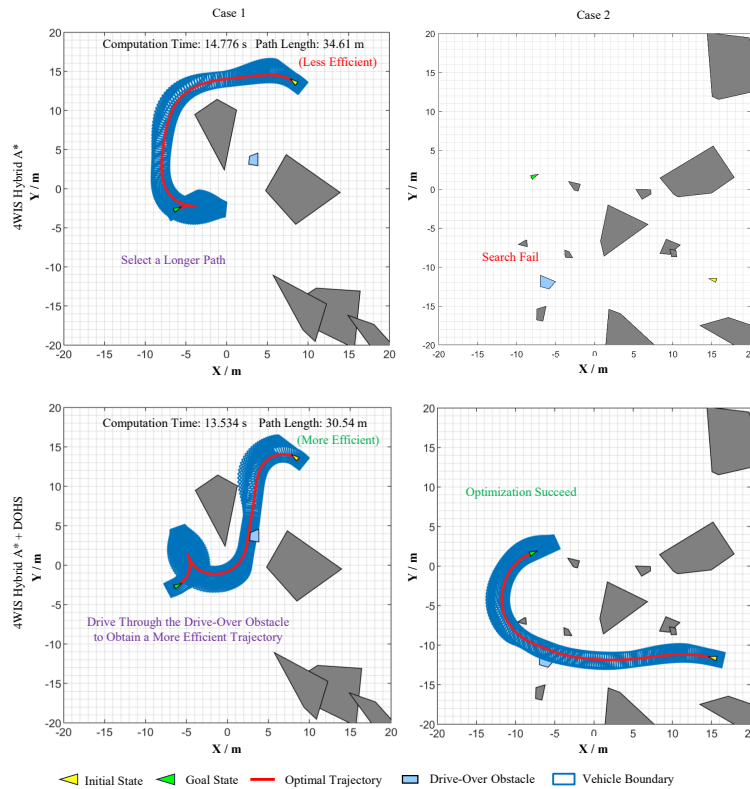


**Figure 11:** Visualization of the 4WIS hybrid A\* algorithm with and without the “drive-over” obstacle handling strategy. In the top row, the 4WIS hybrid A\* avoids all obstacles, leading to a longer path in Case 1 and a planning failure in Case 2. In contrast, the 4WIS hybrid A\* algorithm with the “drive-over” obstacle handling strategy (DOHS) generates shorter and feasible trajectories, demonstrating improved planning efficiency in constrained environments.

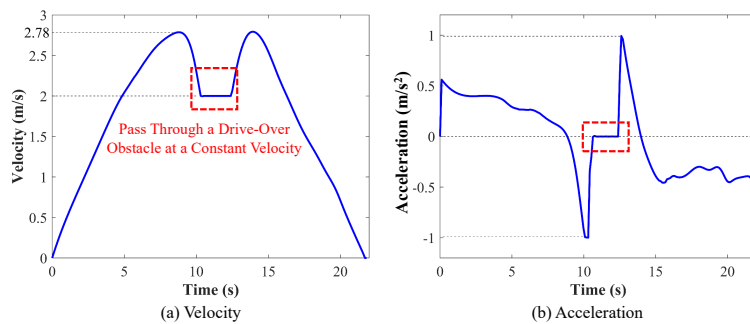


**Figure 12:** Vehicle's velocity and acceleration profiles while traversing a “drive-over” obstacle.